# Characterizing the far-infrared properties of distant X-ray detected AGNs: evidence for evolution in the infrared–X-ray luminosity ratio

J. R. Mullaney,[1][*] D. M. Alexander,[1] M. Huynh,[2] A. D. Goulding[1] and D. Frayer[2]

[1]*Department of Physics and Astronomy, Durham University, South Road, Durham DH1 3LE*
[2]*Infrared Processing and Analysis Center, California Institute of Technology, 100-22, Pasadena, CA 91125, USA*

## ABSTRACT

We investigate the far-infrared (FIR) properties of X-ray sources detected in the *Chandra* Deep Field-South (CDF-S) survey using the ultradeep 70 and 24 μm *Spitzer* observations taken in this field. Since only 30 (i.e. ≈10 per cent) of the 266 X-ray sources in the region of the 70 μm observations are detected at 70 μm, we rely on stacking analyses of the 70 μm data to characterize the average 70 μm properties of the X-ray sources as a function of redshift, X-ray luminosity and X-ray absorption. Using *Spitzer*-IRS data of the *Swift*-Burst Alert Telescope (BAT) sample of $z \approx 0$ active galactic nuclei (AGNs), we show that the 70/24 μm flux ratio can distinguish between AGN-dominated and starburst-dominated systems out to $z \approx 1.5$. Among the X-ray sources detected at 70 μm, we note a large scatter in the observed 70/24 μm flux ratios, spanning almost a factor of 10 at similar redshifts, irrespective of object classification, suggesting a range of AGN:starburst ratios. From stacking analyses we find that the average observed 70/24 μm flux ratios of AGNs out to an average redshift of 1.5 are similar to $z \approx 0$ AGNs with similar X-ray luminosities ($L_X = 10^{42-44}$ erg s$^{-1}$) and absorbing column densities ($N_H \leq 10^{23}$ cm$^{-2}$). Furthermore, both high-redshift and $z \approx 0$ AGNs follow the same tendency towards warmer 70/24 μm colours with increasing X-ray luminosity ($L_X$). From analyses of the *Swift*-BAT sample of $z \approx 0$ AGNs, we note that the 70 μm flux can be used to determine the IR (8–1000 μm) luminosities of high-redshift AGNs. We use this information to show that $L_X = 10^{42-43}$ erg s$^{-1}$ AGNs at high redshifts ($z = 1-2$) have IR to X-ray luminosity ratios ($L_{IR}/L_X$) that are, on average, $4.7^{+10.2}_{-2.0}$ and $12.7^{+7.1}_{-2.6}$ times higher than AGNs with similar X-ray luminosities at $z = 0.5-1$ and $\approx 0$, respectively. By comparison, we find that the $L_{IR}/L_X$ ratios of $L_X = 10^{43-44}$ erg s$^{-1}$ AGNs remain largely unchanged across this same redshift interval. We explore the consequences that these results may have on the identification of distant, potentially Compton-thick AGNs using $L_{IR}/L_X$ ratios. In addition, we discuss possible scenarios for the observed increase in the $L_{IR}/L_X$ ratio with redshift, including changes in the dust covering factor of AGNs and/or the star formation rates of their host galaxies. Finally, we show how deep observations to be undertaken by the *Herschel Space Observatory* will enable us to discriminate between these proposed scenarios and also identify Compton-thick AGNs at high redshifts.

**Key words:** galaxies: active – galaxies: high-redshift – infrared: galaxies – X-rays: galaxies.

# 1 INTRODUCTION

Deep X-ray surveys undertaken by the *Chandra* and *XMM–Newton* observatories have provided the most efficient method to date of identifying large number of active galactic nuclei (AGNs) out to high redshifts ($z \approx 5$; e.g. Alexander et al. 2001; Barger et al. 2003;

Bauer et al. 2004; Szokoly et al. 2004; Brandt & Hasinger 2005; Mainieri et al. 2005). Due to the high penetrating power of hard (i.e. >2 keV) X-rays, they provide a means of identifying AGNs that is much less biased towards unobscured AGNs than, for example, that obtained at optical wavelengths alone. Consequently, deep X-ray surveys have revealed that a large fraction (up to ≈75 per cent; Mainieri et al. 2002; Dwelly & Page 2006; Tozzi et al. 2006; Tajer et al. 2007) of highly obscured AGNs are often unidentified or misclassified by observations at other wavelengths (e.g. Barger et al.

2003; Szokoly et al. 2004). Furthermore, as the central engines of AGNs are the only compact objects capable of producing luminous X-ray emission (i.e. $L_X > 10^{42}$ erg s$^{-1}$), observations at these high energies provide the most reliable method of measuring the intrinsic power of the central engine without suffering from significant contamination by star formation.

Although X-rays provide an ideal means of studying the central engines of AGNs, they yield limited information on the regions outside the central few parsecs. For example, although X-ray observations have been used extensively to measure the amount of absorbing gas (i.e. $N_H$) *along our line of sight* to the central engine (e.g. Mushotzky, Done & Pounds 1993; Bassani et al. 1999; Malizia et al. 2003; Guainazzi, Matt & Perola 2005), they tell us little about the spatial extent and covering factor of the putative obscuring dusty torus, a key component of the unification models that have become a cornerstone of AGN research over the past two decades (e.g. Antonucci & Miller 1985; Krolik & Begelman 1988; Antonucci 1993). Furthermore, as any X-ray emission from stellar processes will be swamped by the presence of an AGN, X-rays alone provide little insight into the relationship between star formation and AGN activity that is predicted by both galaxy formation models (e.g. Kauffmann & Haehnelt 2000; Benson et al. 2003; Granato et al. 2004; Bower et al. 2006; Booth & Schaye 2009) and locally defined black hole–bulge relationships (e.g. Magorrian et al. 1998; Gebhardt et al. 2000; McLure & Dunlop 2002; Tremaine et al. 2002). Observations at infrared (IR) wavelengths can provide significant insights on both these counts.

Like X-rays, the longer IR wavelengths (i.e. $>5\,\mu$m) are largely unaffected by absorption from interstellar gas/dust. However, because IR radiation is typically produced via the reprocessing of shorter wavelength light by dust, it also provides a means to study the dusty environments surrounding AGNs. Furthermore, as both AGNs and starbursting systems are capable of producing large amounts of IR radiation, the study of AGNs at these wavelengths can provide insights into the processes that connects AGN activity and star formation. However, despite considerable gains in our understanding of the IR properties of AGNs since the launch of the *Spitzer Space Telescope*, there remains many unresolved questions. For example, we currently lack a clear picture of how the IR emission of AGNs is affected by the differences in the intrinsic power of the central engine and, perhaps more importantly, whether it evolves over cosmic time. As a result, our understanding of both the putative torus and the interplay between AGN activity and star formation is limited.

To date, most studies of the IR properties of AGNs have concentrated on the relatively short data provided by the Infrared Array Camera (IRAC; 3.6, 4.5, 5.8 and 8.0 μm) and the 24 μm observations taken with the Multiband Imaging Photometer (MIPS) onboard the *Spitzer Space Telescope* (e.g. Lutz et al. 2004; Stern et al. 2005; Daddi et al. 2007; Donley et al. 2007). However, studies of high-redshift objects at these shorter wavelengths are hindered by the presence of strong spectral features at $\lambda\lambda \lesssim 12\,\mu$m [in particular polycyclic aromatic hydrocarbons (PAHs), silicate absorption features and strong emission lines] that shift into these wavebands at $z \gtrsim 0.7$. For example, the IR luminosities of high-redshift galaxies are overestimated by a factor of ∼2–5 (depending on redshift and $L_{IR}$) when using 24 μm data alone compared to that calculated using the full IR spectral energy distribution (SED) incorporating longer wavelength data (at 70 and 160 μm; see Papovich et al. 2007; Magnelli et al. 2009; Magnelli et al., in preparation). Furthermore, as emission from high-redshift starbursting systems peaks at longer wavelengths than those probed by the 24 μm waveband, the sole use of near and mid-IR (MIR) observations hampers our ability to

efficiently distinguish between star formation and AGN-dominated systems. This too can be resolved by incorporating longer wavelength IR data into our analysis. Undoubtedly, the launch of the *Herschel Space Telescope*, with its ability to observe the Universe at 55–672 μm, will help in addressing these issues. However, progress can be made now by applying stacking analyses to deep *Spitzer* 24 and 70 μm observations, enabling us to measure the average IR properties of AGNs at a sensitivity level comparable to that achievable for individual sources in the proposed deep *Herschel* fields (e.g. the HGOODS key programme;[1] PI: D. Elbaz).

In this paper, we investigate the MIR to far-IR (FIR) properties of X-ray detected AGNs that lie in the confusion-limited 70 and 24 μm *Spitzer*-MIPS Far-Infrared Deep Extragalactic Legacy Survey (FIDEL) and Great Observatories Origins Deep Survey (GOODS). We identify AGNs using the 1 Ms *Chandra* Deep Field-South (CDF-S) X-ray observations (which have high-quality X-ray spectral constraints published in Tozzi et al. 2006) and explore their 70 μm fluxes, luminosities and 70/24 μm flux ratios (hereafter $S_{70}/S_{24}$) as a function of redshift, X-ray luminosity and X-ray absorption. As part of our analysis, we use the *Swift*-Burst Alert Telescope (BAT) sample of local, well studied AGNs to develop diagnostics to distinguish between starburst (SB) and AGN-dominated systems at $z \lesssim 1.5$. In the CDF-S field, we find evidence that more X-ray luminous AGNs have warmer, more AGN-dominated IR colours and that high-$z$, low X-ray luminosity (i.e. $z = 1$–2, $L_X = 10^{42-43}$ erg s$^{-1}$) AGNs are significantly more IR luminous than their low-redshift counterparts (i.e. $z = 0.5$–1, $L_X = 10^{42-43}$ erg s$^{-1}$). This increase in IR luminosity may be interpreted as tentative evidence of larger dust covering factors in high-redshift AGNs, supporting results from deep X-ray surveys which find evidence of larger levels of $N_H$ at similar redshifts (e.g. La Franca et al. 2005; Hasinger 2008). However, a proportion of this increase may also be attributed to higher levels of star formation in these systems. We show that deep, FIR *Herschel* surveys will resolve the dominant process behind this increase in IR luminosity and enable the discrimination between AGN and star formation dominated systems out to $z \approx 5$–6.

Throughout this work we adopt $H_0 = 71$ km s$^{-1}$ Mpc$^{-1}$, $\Omega_M = 0.27$ and $\Omega_\Lambda = 0.73$. We report 1$\sigma$ errors for detected sources and provide 3$\sigma$ upper limits for undetected sources ($<3\sigma$).

## 2 DATA

Our main focus throughout this work is the analysis of the MIR and FIR (5–30 and 30–300 μm, respectively) emission of X-ray detected sources in the CDF-S field. To aid in the interpretation of the CDF-S data, we also make use of archival spectra obtained using *Spitzer's* Infrared Spectrograph (IRS) and *IRAS* photometry for the *Swift*-BAT sample of local X-ray AGNs, two archetypal AGNs (NGC 1068 and NGC 6240) and a distant quasi-stellar object (QSO) sample. We describe the CDF-S sample in Section 2.1 and the comparison samples in Section 2.2.

### 2.1 CDF-S sample of X-ray detected AGNs and starbursts

#### 2.1.1 Chandra data

The X-ray data for our main sample are taken from the 1 Ms CDF-S X-ray observations (Giacconi et al. 2002), as analysed by Alexander et al. (2003). In total, there are 201, 304 and 326 X-ray detected

---

[1] URL: http://herschel.esac.esa.int/Docs/KPOT/GOODS_Herschel.pdf
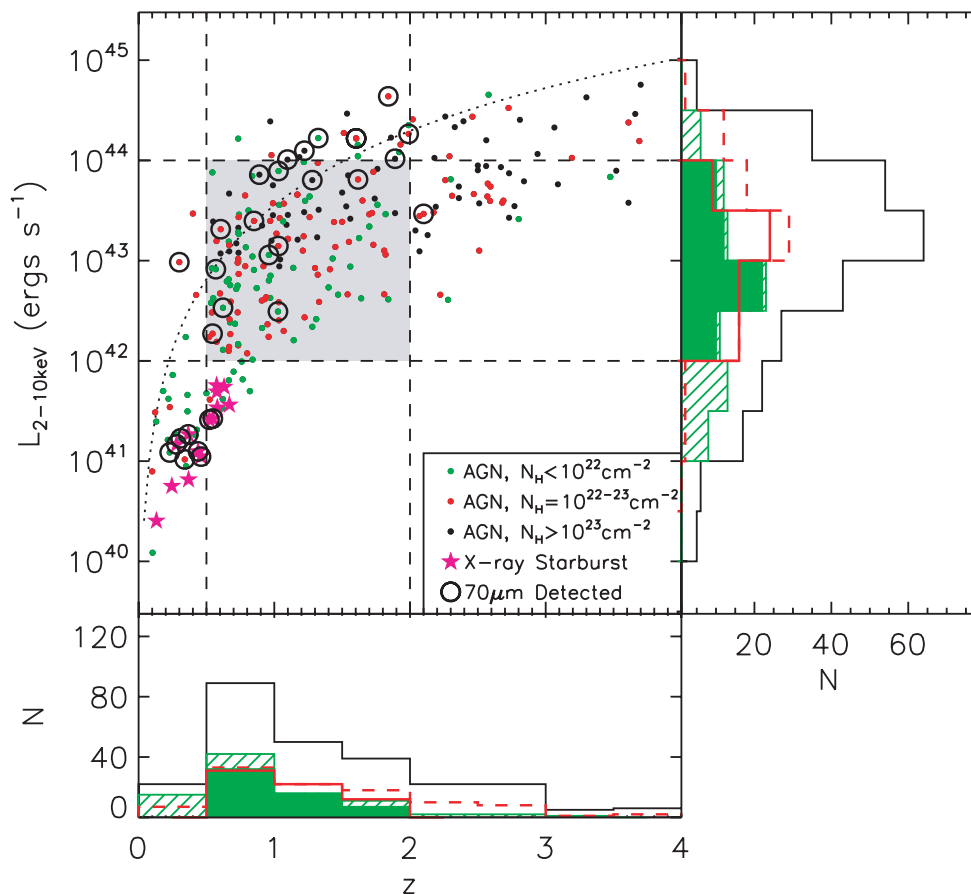
**Figure 1.** Rest-frame hard X-ray luminosity ($L_{2-10\,keV}$) versus redshift ($z$) of the AGNs and SBs identified in the 1 Ms CDF-S X-ray observations, separated according to column density ($N_H$). Those sources detected at 70 μm are indicated with large circles. As described in Section 2.1.1, this sample contains biases in favour of more luminous sources and higher column densities at higher redshifts. To mitigate the effects of these biases, we define a more heterogeneous subsample (the 'Restricted' sample), contained within the grey shaded region. Coloured histograms indicate the number of AGNs in each redshift and X-ray luminosity bin that have column densities $N_H < 10^{22}$ cm$^{-2}$ (green) and $N_H = 10^{22-23}$ cm$^{-2}$ (red). The black histogram shows the distribution of the full AGN + SB sample. Solid colours/lines are used to indicate the restricted sample, hatching/dashes indicate the (unrestricted, flux limited) parent sample. The curved dotted line indicates the constant, unabsorbed hard X-ray flux ($6.8 \times 10^{-15}$ erg s$^{-1}$ cm$^{-2}$) that best fits the $L_X - z$ distribution of the 70 μm detected X-ray AGNs.

objects in this region down to limiting 2–8 keV fluxes of $10^{-15}$, $10^{-16}$ and $10^{-17}$ erg s$^{-1}$ cm$^{-2}$, respectively. The CDF-S data is deep enough to detect star formation activity out to $z \approx 1$. Since the primary aim of this study is to explore the IR properties of X-ray detected AGNs, we have used the Bauer et al. (2004) X-ray source classifications to separate AGNs from star-forming galaxies. In the full catalogue of X-ray sources, there are 288 X-ray AGNs and 15 X-ray SBs (the remaining 23 are classed as either normal galaxies or stars and are excluded from further discussion). The absorption corrected 2–10 keV X-ray luminosities ($L_X$) and X-ray absorption column densities ($N_H$) are taken from Tozzi et al. (2006). Here, we only consider those 266 X-ray AGNs/SBs with well defined $L_X$ and $N_H$ measurements. Spectroscopic and photometric redshifts for these 266 X-ray AGNs/SBs were also taken from Tozzi et al. (2006); 137 have spectroscopic redshifts (113 of which are described as secure, see Tozzi et al. 2006 for details). We use photometric redshifts for the remaining 129 X-ray AGNs/SBs that lack spectroscopic redshifts.

In Fig. 1, we present the $L_X$-redshift distribution of the 266 X-ray AGNs/SBs considered in this study. As is to be expected in flux limited samples, there is a strong bias towards the detection of more luminous sources at higher redshifts. Furthermore, as is shown in
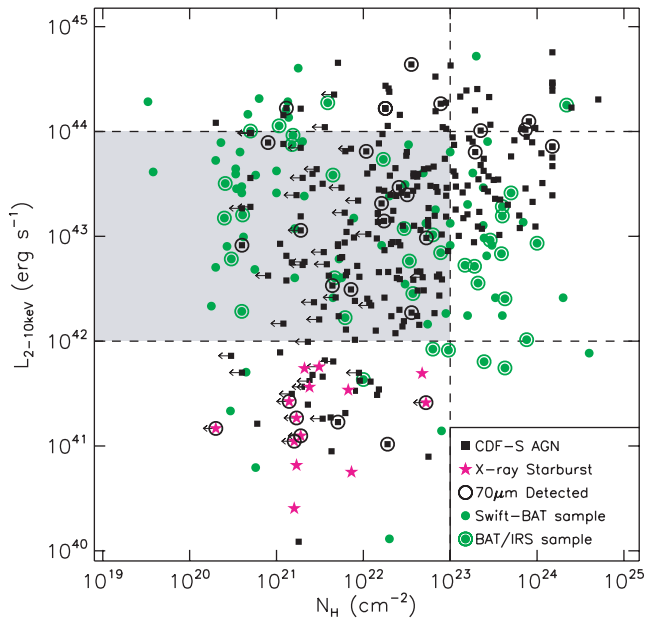
Fig. 2, there is a bias towards higher column densities at higher X-ray luminosities because (i) only the brightest X-ray sources can be detected behind $N_H > 10^{22-23}$ cm$^{-2}$ and (ii) it is difficult to measure low values of $N_H$ at high redshifts due to the absorption cut-off being shifted out of the lowest *Chandra* energy band. In our analysis, we consider two main samples: (i) the full sample of classified X-ray AGNs/SBs and (ii) a 'restricted' sample limited to those AGNs with $L_X = 10^{42-44}$ erg s$^{-1}$ and $N_H < 10^{23}$ cm$^{-2}$ within the redshift range of $0.5 < z < 2.0$ (indicated by the shaded regions in Figs 1 and 2). The 'restricted' sample is used to mitigate the effects of absorption and selection biases on the average results; the $L_X$ and $N_H$ range of the restricted sample is also well matched to the $z \approx 0$ *Swift*-BAT comparison sample (see Section 2.2.1).

### 2.1.2 Spitzer data

The 24 and 70 μm *Spitzer*-MIPS GOODS/CDF-S[2] observations (PID: 20147; P. I.: D. Frayer) and FIDEL[3] legacy surveys (PID:

---

[2] URL: http://www.stsci.edu/science/goods/
[3] URL: http://irsa.ipac.caltech.edu/data/SPITZER/FIDEL/

**Figure 2.** Rest-frame hard X-ray luminosity ($L_{2-10\,\mathrm{keV}}$) versus column density ($N_\mathrm{H}$) of AGNs and SBs identified in the 1 Ms CDF-S X-ray observations. Also shown is the $L_\mathrm{X} - N_\mathrm{H}$ distribution of the *Swift*-BAT sample of $z = 0$ AGNs which covers the same region of the plot as the CDF-S sample. The selection criteria for inclusion in the 'Restricted' sample is indicated by the shaded region.

30948; P. I.: M. Dickinson) are the deepest available at these wavelengths and, therefore, present the best data sets to study the MIR to FIR emission of AGNs in the high-$z$ Universe. While the FIDEL region covers the full E-CDFS (Lehmer et al. 2005), the deepest region is the $10 \times 10$ arcmin$^2$ region centred on the CDF-S field covered by the GOODS observations. The raw 70 μm data were processed off-line using the Germanium Reprocessing Tools (GeRT), following the techniques described in Frayer et al. (2006). The final mosaics, produced by the Mosaicker and Point source Extractor (MOPEX)[4], have a pixel scale of 4.0 arcsec. The 70 μm $3\sigma$ sensitivity is 2.0 mJy in the CDF-S field and $\approx 3.0$ mJy in the outer E-CDFS regions. The 24 μm images produced using MOPEX have a pixel scale of 1.2 arcsec. The sky coverage at 24 μm is inhomogeneous and the sensitivity ranges from 30 to 70 μJy ($5\sigma$). Assuming a SNR of 4.1 for the 24 μm observations (corresponding to a mean flux limit of $\approx 50$ μJy), there are 14 025 detected sources in the FIDEL field.

### 2.1.3 X-ray–IR source matching

We matched the classified X-ray sources to the 70 μm sources assuming a search radius of 2.0 arcsec for those sources in the GOODS field with 24 μm /IRAC counterparts and 4.0 arcsec in the larger FIDEL field. This yields 30 matches which are listed in Table 1, representing $\approx 11$ per cent of the 266 X-ray AGNs/SBs. Using the $P$-statistic [$P = 1 - \exp(-\pi n\theta^2)$; e.g. see Downes et al. 1986 and equation 1 in Pope et al. 2006] and a 70 μm source density $n \approx 2.0 \times 10^3$ deg$^{-2}$, the chance of one or more 70 μm source lying within 4.0 arcsec of an X-ray source is $P \approx$

0.2 per cent. Given the small value of $P$, it was not necessary to apply the correction to the matching procedure described by Downes et al. (1986).

We matched the X-ray sources to the 24 μm sources using a 3.0 arcsec search radius; this search radius was found to provide the best compromise between finding real matches while reducing the number of spurious matches. Out of the 266 CDF-S X-ray AGN/SBs, we found 172 have 24 μm counterparts (i.e. $\approx 65$ per cent). The number of spurious matches in the CDF-S field was estimated to be $\sim 4.5$ per cent using two approaches (i) by calculating the area of the field covered by 24 μm sources, assuming that each source is a circle of radius 3.0 arcsec and (ii) by shifting the positions of the 24 μm sources by a random displacement between 20 and 55 arcsec and then rematching to the X-ray sample. This spurious matching fraction is consistent with the $P$-statistic ($\approx 3$ per cent), assuming $n \approx 1.5 \times 10^4$ deg$^{-2}$ (see above). In spite of the larger $P$-statistic associated with the 24 μm matches compared to the 70 μm matches, the correction described in Downes et al. (1986) need only be applied to 15 (6 per cent) of the 266 X-ray sources and has negligible effect on any of our results.

All but one of the 70 μm detected sources has a 24 μm counterpart. Further investigation reveals that the lack of a matched 24 μm counterpart is the result of the larger point spread function (PSF) of the 70 μm image; at the corresponding position in the 24 μm image there is a cluster of sources that lie just outside the 3.0 arcsec matching radius which blend to form a single 'source' in the 70 μm image. To mitigate source blending, we deblend the 70 μm sources with Gaussians placed at the 24 μm positions. It is these 'deblended' fluxes that are reported in Table 1.

Finally, one of the 70 μm detected X-ray sources lies within 3.0 arcsec of two 24 μm sources (Tozzi et al. 2006, Index: 31); in Table 1, we list both 24 μm matches but assume that the brighter of the two 24 μm sources is the real match in our analysis.

### 2.1.4 24 and 70 μm stacking procedure

As the majority of the X-ray sources are not detected at 70 μm, we rely on stacking analyses to provide insight into their average MIR to FIR properties. Stacking was performed using the code of Huynh et al. (2007). Cutouts of $128 \times 128$ arcsec$^2$ ($32 \times 32$ pixels) were made from the 70 μm image at the stack positions and combined using a weighted mean. The 70 μm stacked flux density was measured using an aperture of 8.0 arcsec at the stacked image centre. Offset stacks were generated using random but nearby offset positions ($<64$ arcsec) in the 70 μm image. 200 randomly offset stacks were made and the uncertainty in the stacked flux is taken as the standard deviation of the measured flux density in the 200 offset stacks.

We created stacks that either include or exclude the 70 μm detected sources; the former (hereafter *'all'*) provides a global average of the FIR properties of all X-ray sources and the latter (hereafter *'undetected'*) provides the average of the 70 μm undetected X-ray sources that is less skewed by individual bright 70 μm sources. We also stack only the 70 μm detected sources for comparison (hereafter *'detected'*). Because the *all* stacks often appear to be dominated by the few 70 μm detected sources we generally use the *detected* and *undetected* stacks in our analysis.

In order to isolate trends between the IR emission from AGNs and other physical properties, we further split the 'Restricted' sample (see Section 2.1.1) in terms of $L_\mathrm{X}(= 10^{42-43}, = 10^{43-44}$ erg s$^{-1}$), $N_\mathrm{H}(<10^{22}, = 10^{22-23}$ cm$^{-2}$) and redshift ($z = 0.5$–1.0, 1.0–2.0).

**Table 1.** The 30 X-ray detected sources with $>3\sigma$ detections at 70 μm.

| (1) T06 | (2) A03 | (3) Name | (4) RA | (5) Dec. | (6) $z$ | (7) $z$ flag | (8) $\log(L_X)$ (ergs s$^{-1}$) | (9) $N_H(10^{22}$ cm$^{-2})$ | (10) $S_{70}$(μJy) | (11) $S_{24}$(μJy) | (12) $\frac{S_{70}}{S_{24}}$ | (13) $L_{IR}(L_\odot)$ | (14) Classification |
|---|---|---|---|---|---|---|---|---|---|---|---|---|---|
| 7 | 312 | J033301.8-275818 | 53.2574 | −27.9718 | 1.840 | 0.6 | 44.64 | 3.57 | 6370 ± 620 | 640 ± 11 | 9.96 ± 0.99 | 12.7 | Abs. Non-BLAGN |
| 29 | 240 | J033239.0-275701 | 53.1626 | −27.9505 | 0.300 | 0.9 | 42.98 | 5.32 | 26 600 ± 2100 | 3239 ± 11 | 8.20 ± 0.64 | 11.2 | Abs. Non-BLAGN |
| 31 | 230 | J033237.9-275213 | 53.1577 | −27.8704 | 1.603 | 3.0 | 44.22 | 1.79 | 3920 ± 430 | 777.4 ± 9.3 | 5.05 ± 0.56 | 12.3 | Abs. Non-BLAGN |
| 31 | 230 | J033237.9-275213 | 53.1577 | −27.8704 | 1.603 | 3.0 | 44.22 | 1.79 | 3920 ± 430 | 248.3 ± 9.3 | 15.8 ± 1.8 | 12.2 | Abs. Non-BLAGN |
| 36 | 204 | J033233.1-274548 | 53.1379 | −27.7634 | 1.030 | 0.5 | 43.15 | 1.73 | 4020 ± 440 | 477 ± 13 | 8.42 ± 0.96 | 11.9 | Abs. Non-BLAGN |
| 44 | 173 | J033226.6-274036 | 53.1108 | −27.6767 | 1.031 | 3.0 | 43.89 | 0.08 | 8010 ± 770 | 2107 ± 15 | 3.80 ± 0.37 | 12.2 | Unabs. BLAGN |
| 46 | 163 | J033225.3-274219 | 53.1052 | −27.7054 | 1.617 | 3.0 | 43.81 | 1.08 | 4580 ± 500 | 485 ± 13 | 9.4 ± 1.1 | 12.6 | Abs. BLAGN |
| 51 | 118 | J033217.3-275221 | 53.0719 | −27.8728 | 1.097 | 3.0 | 44.01 | 22.42 | 4340 ± 740 | 259.2 ± 8.6 | 16.7 ± 2.9 | 11.7 | Abs. Non-BLAGN |
| 52 | 117 | J033217.2-274304 | 53.0718 | −27.7178 | 0.569 | 3.0 | 42.91 | 0.04 | 30 500 ± 2300 | 1247 ± 10 | 24.4 ± 1.9 | 11.7 | Unabs. BLAGN |
| 56 | 88 | J033213.3-274241 | 53.0554 | −27.7115 | 0.605 | 3.0 | 43.31 | 1.62 | 9620 ± 860 | 665 ± 16 | 14.5 ± 1.3 | 11.3 | Abs. Non-BLAGN |
| 69 | 38 | J033201.5-274138 | 53.0063 | −27.6941 | 0.850 | 0.4 | 43.40 | 3.20 | 1600 ± 620 | 356.9 ± 8.9 | 4.5 ± 1.8 | 11.2 | Abs. Non-BLAGN |
| 72 | 30 | J033158.3-275043 | 52.9931 | −27.8453 | 1.990 | 0.5 | 44.26 | 7.77 | 3020 ± 400 | 796.2 ± 9.1 | 3.79 ± 0.50 | 12.4 | Abs. Non-BLAGN |
| 77 | 311 | J033301.7-274543 | 53.2570 | −27.7620 | 0.622 | 3.0 | 42.53 | 0.44 | 5190 ± 540 | 385.7 ± 9.1 | 13.5 ± 1.4 | 11.1 | Unabs. BLAGN |
| 78 | 193 | J033230.1-274524 | 53.1256 | −27.7568 | 0.960 | 3.0 | 43.06 | <0.19 | 6960 ± 640 | 484 ± 12 | 14.4 ± 1.4 | 11.7 | Unabs. BLAGN |
| 98 | 260 | J033244.3-275142 | 53.1846 | −27.8618 | 0.279 | 3.0 | 41.17 | <0.02 | 91 600 ± 6700 | 7020 ± 11 | 13.05 ± 0.95 | 11.5 | Unabs. Starburst |
| 122 | 295 | J033257.7-274549 | 53.2404 | −27.7636 | 2.100 | 0.5 | 43.47 | 2.58 | 4030 ± 460 | – | – | – | Abs. Non-BLAGN |
| 152 | 302 | J033259.4-274859 | 53.2476 | −27.8165 | 1.280 | 0.6 | 43.80 | 19.41 | 3620 ± 430 | 769 ± 11 | 4.71 ± 0.56 | 12.0 | Abs. Non-BLAGN |
| 155 | 60 | J033208.0-274240 | 53.0335 | −27.7111 | 0.545 | 3.0 | 42.27 | 3.59 | 2880 ± 410 | 455 ± 10 | 6.33 ± 0.92 | 10.9 | Abs. Non-BLAGN |
| 175 | 284 | J033252.0-274437 | 53.2165 | −27.7438 | 0.522 | 3.0 | 41.41 | <−5.26 | 5770 ± 580 | 1213 ± 11 | 4.76 ± 0.48 | 11.2 | Abs. Starburst |
| 206 | 109 | J033216.3-273930 | 53.0678 | −27.6586 | 1.324 | 3.0 | 44.22 | 0.13 | 5100 ± 540 | 1376 ± 12 | 3.71 ± 0.39 | 12.2 | Unabs. BLAGN |
| 242 | 285 | J033251.9-274229 | 53.2164 | −27.7083 | 1.027 | 3.0 | 42.49 | 0.72 | 8150 ± 750 | 500 ± 11 | 16.3 ± 1.5 | 11.9 | Unabs. Non-BLAGN |
| 253 | 131 | J033220.1-274448 | 53.0839 | −27.7467 | 1.890 | 1.9 | 44.02 | 73.51 | 3160 ± 380 | 327.20 ± 0.20 | 9.6 ± 1.2 | 12.4 | Abs. Non-BLAGN |
| 268 | 278 | J033249.3-274050 | 53.2056 | −27.6806 | 1.222 | 3.0 | 44.10 | 80.44 | 4850 ± 520 | 2127 ± 16 | 2.28 ± 0.25 | 12.1 | Abs. Non-BLAGN |
| 525 | 129 | J033219.9-274123 | 53.0828 | −27.6899 | 0.229 | 3.0 | 41.09 | 0.00 | 14 000 ± 1200 | 2932 ± 17 | 4.79 ± 0.41 | 10.7 | Unabs. Non-BLAGN |
| 538 | 65 | J033208.6-274649 | 53.0359 | −27.7803 | 0.310 | 3.0 | 41.23 | 0.51 | 12 900 ± 1100 | 973 ± 14 | 13.2 ± 1.1 | 10.7 | Unabs. Non-BLAGN |
| 553 | 292 | J033256.8-275318 | 53.2366 | −27.8885 | 0.366 | 3.0 | 41.27 | <−0.17 | 8520 ± 770 | 612.3 ± 7.1 | 13.9 ± 1.3 | 10.7 | Unabs. Starburst |
| 567 | 236 | J033238.9-274732 | 53.1620 | −27.7925 | 0.460 | 3.0 | 41.05 | <0.16 | 6370 ± 600 | 730.9 ± 8.9 | 8.72 ± 0.83 | 11.1 | Unabs. Starburst |
| 575 | 115 | J033217.2-274922 | 53.0715 | −27.8230 | 0.340 | 3.0 | 41.02 | 1.90 | 3290 ± 370 | 221.5 ± 9.5 | 14.8 ± 1.8 | 10.2 | Abs. Non-BLAGN |
| 577 | 224 | J033236.3-274933 | 53.1512 | −27.8258 | 0.547 | 3.0 | 41.42 | <−0.14 | 10 470 ± 890 | 664 ± 10 | 15.8 ± 1.4 | 11.2 | Unabs. Starburst |
| 608 | 318 | J033304.0-275027 | 53.2665 | −27.8409 | 0.890 | 3.0 | 43.86 | 150.00 | 3090 ± 410 | 578.0 ± 9.3 | 5.34 ± 0.71 | 11.6 | Abs. Non-BLAGN |
| 646 | 266 | J033245.2-274724 | 53.1884 | −27.7903 | 0.438 | 3.0 | 41.10 | <0.19 | 11 700 ± 1600 | 507.2 ± 8.6 | 23.1 ± 3.2 | 11.0 | Unabs. Starburst |

*Notes.* (1) Source index from Tozzi et al. (2006); (2) source index from Alexander et al. (2003); (3) source name; (4–5) X-ray position (J2000); (6) source redshift; (7) redshift flag; (8) intrinsic (i.e. corrected for absorption) 2–10 keV luminosity; (9) column density in units of $10^{22}$ cm$^{-2}$; (10) 70 μm flux; (11) 24 μm flux; (12) 70/24 μm flux ratio; (13) $L_{IR}$ derived from the 70 μm flux using the method described in the text; (14) Classification from Bauer et al. (2004); and information in columns (1), (3)–(9) are taken from Tozzi et al. (2006).

## 2.2 Comparison samples

In our analysis, we compare the results from the sample of CDF-S X-ray AGNs/SBs to the IR properties of two archetypal AGNs, a sample of bright QSOs from Richards et al. (2006) and, most importantly, a sample derived from local ($z < 0.1$) AGNs in the *Swift*-BAT catalogue of hard X-ray detected AGNs (see Section 2.2.1, Appendix and Tueller et al. 2008). For the latter, we selected those AGNs that cover the same range of X-ray properties (i.e. $L_X$ and $N_H$; see Fig. 2) as the CDF-S X-ray AGNs sample and also have archival *Spitzer*-IRS spectra and/or *IRAS* flux density measurements. The result is a sample that is *directly comparable* to the more distant CDF-S AGNs, but which has far superior IR data due to the relative proximity of the sources.

### 2.2.1 The Swift-BAT sample

The *Swift* telescope is currently undertaking a survey of X-ray bright ($F_{14-195\,keV} \gtrsim 5 \times 10^{-11}\,erg\,s^{-1}\,cm^{-2}$) AGNs using its on-board (BAT); the second data release (DR2) of this survey has recently been published in Tueller et al. (2008). As the BAT instrument is sensitive only to very hard X-rays (14–195 keV), this survey has resulted in a sample of local[5] AGNs that is largely unaffected by absorption (to $N_H < 10^{24}\,cm^{-2}$). The $L_X$ and $N_H$ distributions of the 104 AGNs for which archival 2–10 keV data exist (Bassani et al. 1999; Winter et al. 2009) are comparable to the CDF-S sample (see figs 7 and 10 of Winter et al. 2009). Of these 104 AGNs, 61 have flux density measurements from all four *IRAS* bands (these 61 objects are hereafter referred to as the BAT/*IRAS* sample) which we convert to $L_{IR}$ using equations (2) and (3) in table 1 of Sanders & Mirabel (1996). A search of the *Spitzer* archives reveals that 36 of the 104 AGNs with 2–10 keV data have *Spitzer*-IRS spectroscopy between 5.2–38 μm (these 36 objects are hereafter referred to as the BAT/IRS sample) which we use in conjunction with *IRAS* data to derive the expected observed 24 and 70 μm fluxes at the redshifts covered by the CDF-S sample. All of the AGNs in the BAT/IRS sample are also in the BAT/*IRAS* sample (see Appendix for full details of the IRS/*IRAS* analysis).

On separating the BAT/IRS sample into SB- and AGN-dominated objects, we find that the $S_{70}/S_{24}$ ratio is able to discriminate between these two types of sources out to $z \approx 1.5$ (see shaded regions in Fig. 4 and Appendix). Furthermore, we note that the 70 μm flux density can predict the IR luminosities of all the BAT/IRS objects (i.e. both SB- and AGN-dominated AGNs), as well as the SB galaxies described in Brandl et al. (2006), to within a factor of $\approx 3$. This compares to a factor of $\approx 12$ uncertainty in $L_{IR}$ using 24 μm flux densities alone (see Appendix and Fig. A3).

In the plots that follow, we indicate the average IR properties of the BAT/IRS sample using red and blue lines for the AGN- and SB-dominated systems, respectively. Shading is used to indicate the range of MIR and FIR properties of the BAT/IRS sample.

### 2.2.2 NGC 1068, NGC 6240 and the QSO sample

In addition to the BAT/IRS sample, we also compare the CDF-S AGNs with two well-studied heavily obscured AGNs, NGC 1068

and NGC 6240. The former is regarded as the 'quintessential' type II AGN, showing evidence of a hidden broad-line region in polarized light (e.g. Antonucci & Miller 1985); the latter is a heavily obscured AGN that is SB-dominated at IR wavelengths and is often cited to characterize the properties of faint X-ray AGNs. The tracks for these AGNs were derived from archival *Spitzer*-IRS spectra following the same procedure as used for the BAT/IRS sample as outlined in the Appendix.

Finally, we use the average QSO SED of Richards et al. (2006) to give an indication of the typical IR properties of luminous, unobscured type I AGNs.

We stress that the comparison samples considered here do not cover the full range of SEDs seen in the general galaxy population. It is known, for example, that very strongly starbursting systems have larger $S_{70}/S_{24}$ flux ratios than NGC 6240 (e.g. Arp 220). Furthermore, some quiescent galaxies are known to have low $S_{70}/S_{24}$ flux ratios similar to those of AGNs in the BAT/IRS sample (see Alexander et al., in preparation). However, our main aim here is to explore the IR emission of AGNs with X-ray properties comparable to the CDF-S AGNs, which excludes such extreme systems. We find that the known starbursting systems, such as those presented in Brandl et al. (2006), all produce expected $S_{70}/S_{24}$ flux ratios either consistent with or higher than those of the SB-dominated BAT/IRS AGNs, as indicated by the shaded region in Fig. A3.

## 3 RESULTS

In our analysis, we investigate the IR properties of the CDF-S X-ray AGNs and SBs, including the $S_{70}/S_{24}$ flux ratios, the IR luminosities and the IR−X-ray luminosity ratios. To aid in our analysis, we compare the properties of the CDF-S X-ray sources with expectations based on the more detailed analysis of nearby AGNs with the same X-ray properties as the CDF-S sample (i.e. $L_X$; $N_H$). Since only a minority of CDF-S X-ray AGNs are detected at 70 μm, our analyses rely significantly on 70 μm stacking analyses and the 24 μm fluxes of individual sources.

### 3.1 Individual 70 μm detected sources

#### 3.1.1 X-Ray properties and redshift distribution

In Fig. 1, we show the X-ray luminosity–redshift distribution for the CDF-S X-ray AGNs/SBs and highlight the 70 μm detected objects. As might be expected, there is a preference for bright X-ray AGNs to be detected at 70 μm. However, there are up to two orders of magnitude difference in $L_X$ for 70 μm detected sources at the same redshift, suggesting a large range of X-ray/IR luminosity ratios. As we show in Fig. 3, detection at 70 μm is strongly dependent on the 24 μm flux density. None of the AGNs with $S_{24} < 200\,μJy$, and fewer than a quarter (10/45; $\approx 22$ per cent) of those with $200 < S_{24}/μJy < 500$, are detected at 70 μm. Conversely, the majority (19/28; $\approx 68$ per cent) of those AGNs with $S_{24} > 500\,μJy$ are detected at 70 μm.

The 70 μm detected sources span a broad range of X-ray properties. Of the 29 sources detected at both 70 and 24 μm, 15 ($\approx 52$ per cent) are non-broad-line AGNs (non-BLAGNs), six ($\approx 21$ per cent) are broad-line AGNs (BLAGNs) and eight ($\approx 28$ per cent) are X-ray detected SBs. These 70 μm detected sources comprise 15/218 ($\approx 7$ per cent) of the non-BLAGNs, 6/34 ($\approx 18$ per cent) of BLAGNs and 6/14 ($\approx 43$ per cent) of the X-ray detected SBs; the bias towards the BLAGNs and X-ray detected SBs could

---

[5] 135 of the 153 AGNs with measured redshifts in the BAT sample (presented in Tueller et al. 2008) have $z < 0.1$.
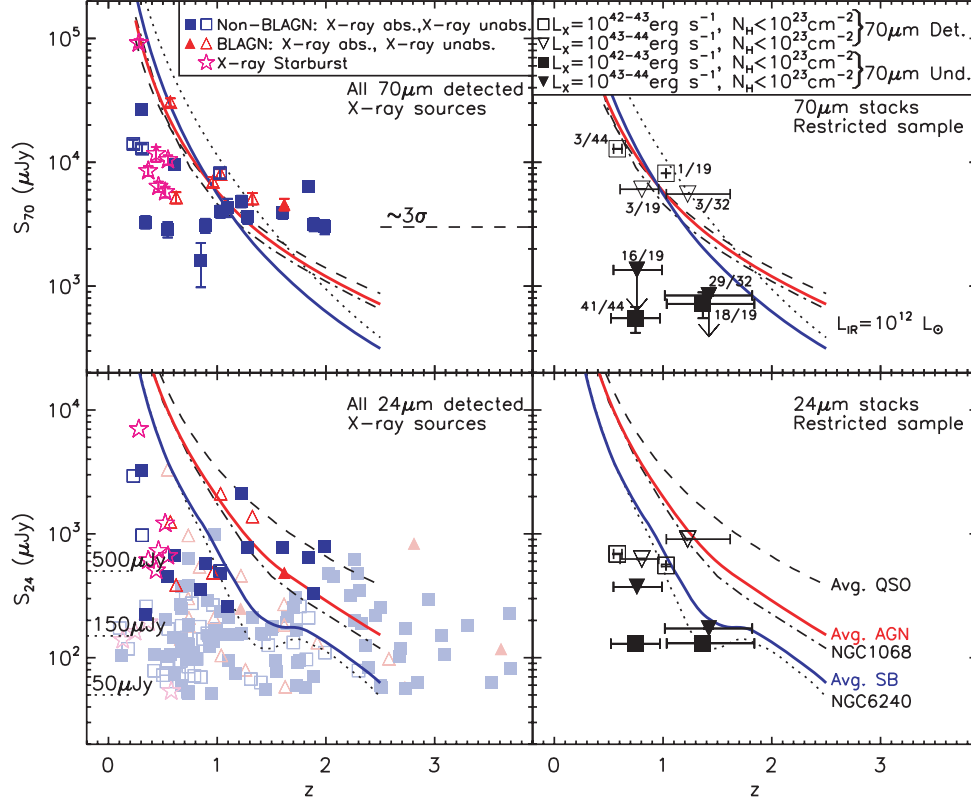
**Figure 3.** Left-hand panels: 70 μm (top) and 24 μm (bottom) flux densities of the CDF-S X-ray SBs and AGNs that are detected in both the 70 and 24 μm wavebands (strong colours) and only the 24 μm waveband (faint colours). Right-hand panels: the average 70 μm (top) and 24 μm (bottom) flux densities of the 70 μm *detected* and 70 μm *undetected* AGNs in the 'Restricted' sample, split according to $L_X$ and $z$. These averages are derived from stacking analyses. The fractions indicate the number of AGNs in each stack as well as in the whole subsample. The five tracks in each panel show the expected flux densities of the comparison AGNs, normalized to $L_{IR} = 10^{12} L_{\odot}$, at $z = 0.25$–2.5.

be due to the BLAGNs and SBs having high $L_X$ and large IR–X-ray luminosity ratios, respectively. The 70 μm detection of AGNs shows no apparent dependency on absorbing column density: for example, at $z < 1.5$, 6/17 ($\approx$35 per cent) 70 μm detected sources are unabsorbed ($N_H < 10^{22}$ cm$^{-2}$), 5/17 ($\approx$29 per cent) are absorbed ($N_H \approx 10^{22} - 10^{23}$ cm$^{-2}$) and 6/17 ($\approx$35 per cent) are heavily absorbed ($N_H > 10^{23}$ cm$^{-2}$).

### 3.1.2 Distinguishing between SB- and AGN-dominated systems

In Fig. 4, we show the $S_{70}/S_{24}$ flux ratios of all of the CDF-S X-ray AGNs/SBs and compare them to the range expected for the BAT/IRS AGN sample and the well studied local AGNs and quasars (see Section 2.2.1 and Appendix). The $S_{70}/S_{24}$ flux ratio provides an effective discrimination between those AGNs with AGN- or SB-dominated IR SEDs to $z \approx 1$–1.5. Using the tracks derived for the BAT/IRS sample, we find that 15/23 ($\approx$65 per cent) and 5/23 ($\approx$22 per cent) of the 70 μm detected CDF-S AGNs have $S_{70}/S_{24}$ flux ratios consistent with SB- and AGN-dominated systems, respectively; the remaining three 70 μm detected AGNs lie in regions of the $S_{70}/S_{24} - z$ plot that are consistent with either SB- or AGN-dominated systems. 10 ($\approx$ 42 per cent) of the 70 μm detected CDF-S AGNs have $S_{70}/S_{24}$ flux ratios within a factor of 1.5 of the NGC 6240 track, five of which are X-ray absorbed and five of which are X-ray unabsorbed. The maximum $S_{70}/S_{24}$ flux ratio of the 70 μm detected sources is $24.4 \pm 1.9$. This is marginally

inconsistent with Papovich et al. (2007) who found 3/30 ($\approx$10 per cent) X-ray detected AGNs in their 70 μm selected sample with $S_{70}/S_{24} > 30$. However, the larger area covered by their survey increases the likelihood of finding rare AGNs with more extreme $S_{70}/S_{24}$ flux ratios that are not represented by our comparison samples (see Section 2.2).

Among the 70 μm detected sources, we find no difference in $S_{70}/S_{24}$ flux ratio between BLAGNs and non-BLAGNs, nor between X-ray absorbed and X-ray unabsorbed AGNs (i.e. $N_H \geq 10^{22}$ cm$^{-2}$ and $N_H < 10^{22}$ cm$^{-2}$, respectively), implying that the material that absorbs photons at X-ray and optical wavelengths is optically thin to rest-frame MIR–FIR radiation (see Section 3.1.1). The average $S_{70}/S_{24}$ flux ratios and redshifts of the absorbed (unabsorbed) 70 μm detected AGNs are $\overline{S_{70}/S_{24}} = 8.2 \pm 4.3 (11.8 \pm 7.3)$ and $\bar{z} = 1.1 \pm 0.6 (0.76 \pm 0.56)$,[6] respectively.

All six 70 μm detected X-ray SBs have $S_{70}/S_{24}$ flux ratios consistent with that expected of SB-dominated systems. However, one of the SBs has a $S_{70}/S_{24}$ flux ratio larger than that expected from the BAT/IRS sample and is typical of the extreme SB systems presented in Brandl et al. (2006) {see Fig. A3}. The 70 μm detected X-ray SBs also span the same range of $S_{70}/S_{24}$ flux ratios as the seven 70 μm detected X-ray AGNs that lie in the same redshift interval (i.e. $z = 0.2$–0.7), providing further evidence that these AGNs have SB-dominated IR SEDs.

---

[6] Given errors correspond to the standard deviation in the stacked flux.
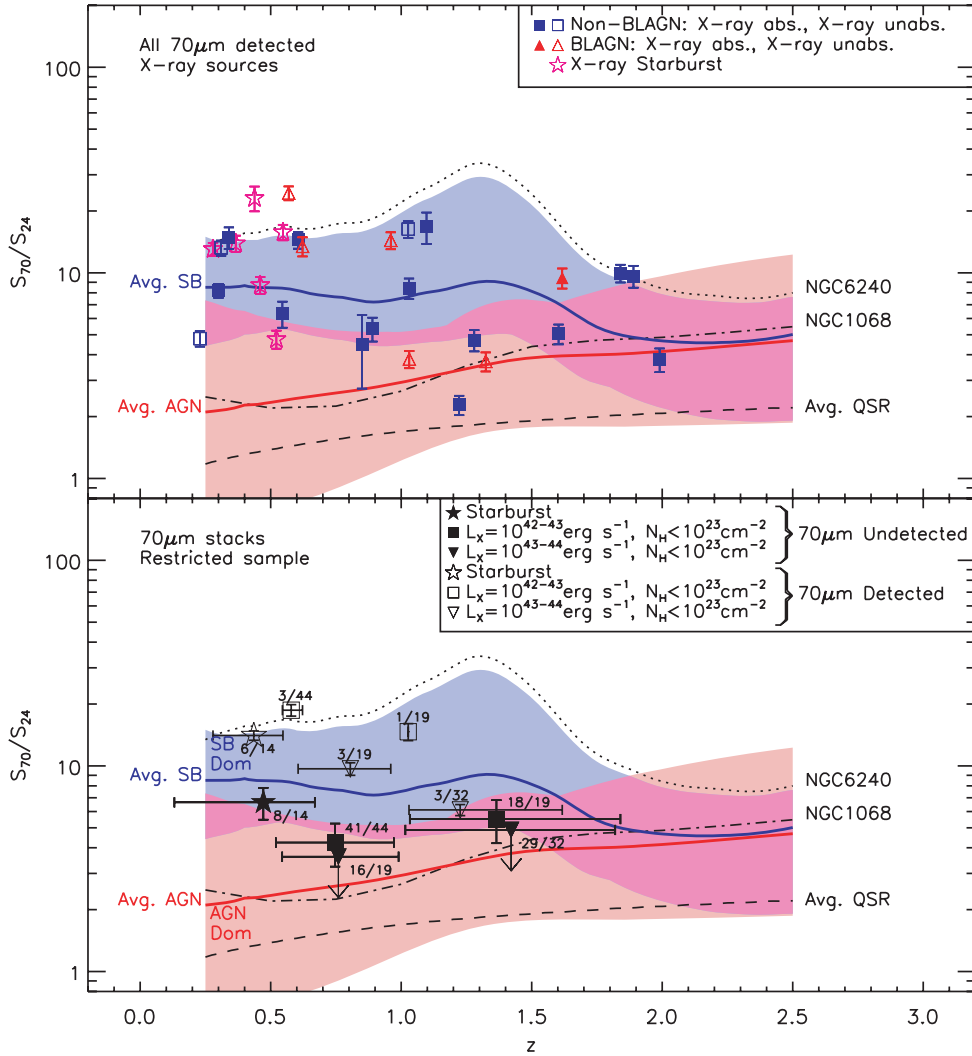
**Figure 4.** Top: $S_{70}/S_{24}$ flux ratios of the CDF-S X-ray AGNs/SBs that are detected at 70 μm. Bottom: the average $S_{70}/S_{24}$ flux ratios of the 70 μm *detected* and 70 μm *undetected* AGNs in the 'Restricted' sample, split according to $L_X$ and $z$. These averages are derived from stacking analyses. The fractions indicate the number of AGNs in each stack as well as in the whole subsample. The five tracks indicate the expected $S_{70}/S_{24}$ flux ratios of the comparison AGNs at $z = 0.25$–2.5; see Section 2.2 and Appendix. The shaded regions indicate the range of expected $S_{70}/S_{24}$ flux ratios of the AGNs in the BAT/IRS sample throughout the redshift range, $z = 0.25$–2.5.

### 3.1.3 IR fluxes and luminosities of individual, 70 μm-detected AGNs

Since we can provide a good characterization of the basic IR SEDs of the 70 μm detected CDF-S X-ray AGNs, we can accurately estimate their IR luminosities. We derive $L_{IR}$ for the 70 μm detected sources by first selecting one of the five tracks plotted in Fig. 4 that best matches the $S_{70}/S_{24}$ flux ratio of a given CDF-S X-ray AGN, then scaling its IR luminosity to reproduce $S_{70}$ of the CDF-S source if observed at the same redshift. Estimating $L_{IR}$ in this manner assumes that the IR SEDs of AGNs at the redshifts covered by the CDF-S observations are similar to those seen in the comparison AGN samples. We take some confidence that this is indeed the case as the range of $S_{70}/S_{24}$ flux ratios of the 70 μm detected subsample is largely bounded by the tracks of our comparison sample.

In the left-hand panel of Fig. 5, we show the $L_{IR}$ of the 70 μm detected sample plotted as a function of $L_X$. We find no significant difference in $L_{IR}$ between BLAGNs and non-BLAGNs or between X-ray absorbed and unabsorbed AGNs. This independence of $L_{IR}$ on

classification provides further supporting evidence that the material that absorbs photons at X-ray and optical wavelengths is optically thin to rest-frame MIR–FIR radiation (see Sections 3.1.1 and 3.1.2). The 70 μm detected CDF-S X-ray AGNs are typically more IR luminous than their counterparts in the BAT/*IRAS* sample of local AGN. This result may be due to the low sensitivity of the 70 μm observations, which could lead to a bias towards the detection of the most IR-luminous AGNs; indeed, the range of IR luminosities ($\approx 2$ orders of magnitude) for the CDF-S X-ray AGNs is narrower than the range of X-ray luminosities ($\approx 3$ orders of magnitude). Overall, the IR to X-ray luminosity ratios ($L_{IR}/L_X$) of the 70 μm detected CDF-S AGNs/SBs span almost 2 orders of magnitude.

The 70 μm detected X-ray SBs have higher $L_{IR}/L_X$ ratios than the majority (20/22; $\approx 91$ per cent) of the 70 μm detected X-ray AGNs. We find all three 70 μm detected X-ray AGNs with $L_X < 10^{41}$ erg s$^{-1}$ have $L_{IR}/L_X$ ratios and $S_{70}/S_{24}$ flux ratios comparable to the 70 μm detected X-ray SBs (Tozzi et al. 2006, Index: 525, 538, 575; see Table 1). However, two of these sources (Index: 525, 538) have optical spectra consistent with AGNs (Szokoly et al. 2004)
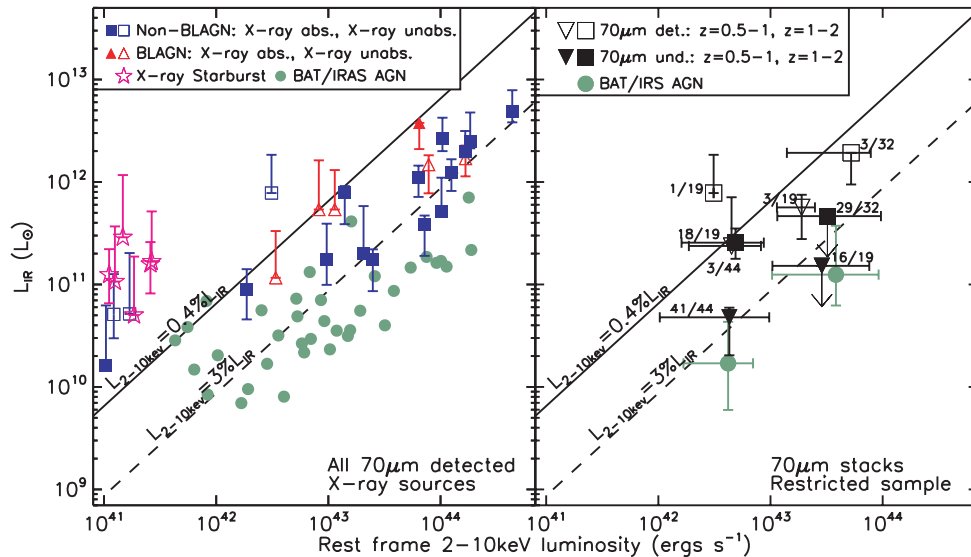
**Figure 5.** $L_{IR}$ versus $L_X$ of the 70 μm detected CDF-S X-ray AGNs/SBs (left-hand panel) and the 70 μm *undetected* and 70 μm *detected* stacks of the 'Restricted' sample, separated according to redshift (right-hand panel). In both plots, the vertical error bars indicate the range of $L_{IR}$ produced by assuming the full range of tracks in Figs 3 and 4 and horizontal error bars indicate the full range of $L_X$ in each stack. For comparison, we include the BAT/*IRAS* AGNs (see Section 2.2.1) and lines of constant $L_{IR}/L_X$ for the average QSO of Elvis et al. (1994; $L_X = 3$ per cent$L_{IR}$) and the AGN-hosting submillimeter galaxies of Alexander et al. (2005; $L_X = 0.4$ per cent $L_{IR}$). For the average BAT/*IRAS* points, we only include BAT/*IRAS* AGNs with X-ray properties matching those of the 'Restricted' sample (i.e. $L_X = 10^{42-44}$ erg s$^{-1}$, $N_H < 10^{23}$ cm$^{-2}$).

while the remainder (Index: 575) has a flat X-ray spectral index in the deeper 2 Ms CDF-S catalogue ($\Gamma < 0.1$; Luo et al. 2008). While this confirms their classification as AGNs, it is clear that their IR SEDs are SB dominated.

As only a small fraction of the CDF-S X-ray AGN sample is detected at 70 μm, we are unable to reliably constrain the IR properties of the majority of the CDF-S X-ray AGNs/SBs using the 70 μm data alone. To better characterize the IR properties for the majority of the CDF-S X-ray AGNs, we therefore use stacking analyses.

### 3.2 24 and 70 μm stacking analysis

The advantage of stacking analyses is that it provides the average properties of sources that lie below the individual source detection limit. However, naturally, information is lost on the fluxes of individual sources. We also stacked the 70 and 24 μm data following the procedure outlined in Section 2.1.4 and present the results in Table 2; although the majority of the CDF-S X-ray sources are detected at 24 μm, we stacked the 24 μm data to provide flux density constraints consistent with those obtained at 70 μm. For completeness, we report the results from stacking the whole sample as well as a range of subsamples (split into bins of $L_X$, $N_H$, $z$, 24 μm flux density, and object classification). As noted in Section 2.1.4, we stacked all X-ray sources in each subsample ('*all*'), and also stacked only the 70 μm detected objects ('*detected*') and only the 70 μm undetected objects ('*undetected*'). The majority of our analyses will focus on the 'Restricted' sample to reduce selection and sensitivity biases (see Section 2.1.1).

All of the CDF-S X-ray sample is detected significantly in the 70 μm stacks, with an average flux density of $S_{70} = 4824 \pm 210$ μJy. Significant detections (S/N > 3) are also found from 70 μm stacking analyses for the majority of the subsamples; however, we note that only 9 ($\approx$50 per cent) of the eighteen 70 μm *undetected* subsamples are significantly detected. From stacking the CDF-S X-ray sample in bins of 24 μm flux density (i.e. $S_{24} =$

50–150, 150–500 and $\geq$500 μJy), we find that the 70 μm flux density and the significance of the detection is positively correlated with the 24 μm flux density of the stacked sources, confirming our previous result for the 70 μm detected sources (see Section 3.1).

We find that when the 'Restricted' sample is stacked in bins of $N_H$ and $z$ (i.e. stacks 5, 6, 7 and 8 in Table 2) only one 70 μm *undetected* stack is detected at 70 μm at a significance $>3\sigma$. The upper limits for these non-detections reveal no significant differences in the IR properties of these subsamples; they are all consistent with $S_{70}/S_{24} \approx 4$ and $L_{IR} \approx 10^{11}$ L$_\odot$. The lack of any significant difference between these stacks may be interpreted as providing further tentative evidence that the material that absorbs X-rays is optically thin to rest-frame MIR–FIR radiation (see Sections 3.1.1, 3.1.2 and 3.1.3). Similarly, none of the $L_X = 10^{43-44}$ erg s$^{-1}$, 70 μm *undetected* stacks (rows 13 and 14 of Table 2) are detected at $>3\sigma$ in either redshift bin ($z = 0.5$–1 and 1–2). However, in this case, the upper limits *do* provide significant insight into the IR properties of the CDF-S X-ray AGNs, revealing that high $L_X$ AGNs have, on average, warmer $S_{70}/S_{24}$ flux ratios than their low $L_X$ counterparts (as discussed in Section 3.2.1).

We proceed with the analysis of the stacked data following a similar procedure as outlined in Section 3.1 for the 70 μm detected sources.

### 3.2.1 SB/AGN contribution to the average IR emission of AGNs

In the lower panel of Fig. 4, we show the $S_{70}/S_{24}$ flux ratios of the 'Restricted' subsamples split in terms of $L_X$ and $z$ (rows 11, 12, 13 and 14 of Table 2). We find that the average $S_{70}/S_{24}$ flux ratios of all four 70 μm *undetected* stacks lie within the range of $S_{70}/S_{24}$ flux ratios expected for the BAT/IRS AGNs out to $z \approx$ 2.5, and run roughly parallel to the average AGN-dominated and average SB-dominated tracks (see Section 2.2.1 and Appendix). The simplest interpretation of this result is that there is little change in the average IR colour with redshift for AGNs in both the

**Table 2.** Descriptions and average properties of the AGN and SB stacks.

| (1) Index | (2) Description | (3) $N$ | | | (4) Mean $z$ | | | (5) $\log(\overline{L_X})$ (ergs s$^{-1}$) | | | (6) Stacked $S_{70}$ (μJy) | | | (7) Stacked $S_{24}$ (μJy) | | | (8) $L_{IR}$ ($L_\odot$) | | |
|---|---|---|---|---|---|---|---|---|---|---|---|---|---|---|---|---|---|---|---|
| | | All | Det. | Und. | All | Det. | Und. | All | Det. | Und. | All | Det. | Und. | All | Det. | Und. | All | Det. | Und. |
| 1 | *Starbursts* | 14 | 6 | 8 | 0.46 | 0.44 | 0.47 | 41.41 | 41.26 | 41.49 | 9960 ± 500 | 22 400 ± 1200 | 630 ± 110 | 736.8 | 1592.9 | 94.7 | 11.0 | 11.3 | 10.1 |
| 2 | $z < 1$ $L_X = 10^{41-42}$ | 25 | 3 | 22 | 0.43 | 0.29 | 0.45 | 41.60 | 41.12 | 41.64 | 1540 ± 160 | 10 070 ± 550 | 380 ± 170 | 235.7 | 1183.5 | 106.4 | 10.4 | 10.8 | <10.5 |
| 3 | $z > 3$ | 12 | 0 | 12 | 3.52 | – | 3.52 | 44.31 | – | 44.31 | 280 ± 180 | – | 280 ± 180 | 127.5 | – | 127.5 | – | – | – |
| 4 | *BLAGN* | 34 | 6 | 28 | 1.54 | 1.02 | 1.65 | 43.94 | 43.74 | 43.97 | 2050 ± 150 | 10 050 ± 450 | 330 ± 160 | 419.3 | 957.3 | 304.1 | 12.0 | 12.3 | <11.9 |
| 5 | $z = 0.5$–$1$ $L_X = 10^{42-44}$ $N_H < 10^{22}$ | 32 | 3 | 29 | 0.74 | 0.72 | 0.74 | 43.10 | 42.88 | 43.12 | 2180 ± 170 | 14 200 ± 830 | 940 ± 170 | 301.6 | 820.2 | 247.9 | 11.2 | 11.7 | 10.9 |
| 6 | $z = 1$–$2$ $L_X = 10^{42-44}$ $N_H < 10^{22}$ | 19 | 2 | 17 | 1.38 | 1.03 | 1.42 | 43.39 | 43.61 | 43.35 | 1230 ± 160 | 8080 ± 540 | 420 ± 170 | 265.0 | 1156.6 | 160.1 | 11.7 | 12.2 | <11.7 |
| 7 | $z = 0.5$–$1$ $L_X = 10^{42-44}$ $N_H = 10^{22-23}$ | 31 | 3 | 28 | 0.75 | 0.67 | 0.76 | 42.99 | 43.20 | 42.96 | 750 ± 140 | 4700 ± 380 | 330 ± 150 | 180.0 | 494.0 | 146.3 | 10.8 | 11.4 | <10.9 |
| 8 | $z = 1$–$2$ $L_X = 10^{42-44}$ $N_H = 10^{22-23}$ | 32 | 2 | 30 | 1.38 | 1.32 | 1.39 | 43.35 | 43.59 | 43.33 | 680 ± 140 | 4300 ± 330 | 440 ± 150 | 174.4 | 480.3 | 154.0 | 11.4 | 12.3 | <11.7 |
| 9 | $z = 0.5$–$1$ $L_X = 10^{42-44}$ $N_H < 10^{23}$ | 63 | 6 | 57 | 0.74 | 0.69 | 0.75 | 43.05 | 43.07 | 43.05 | 1440 ± 110 | 9450 ± 460 | 600 ± 110 | 241.7 | 657.1 | 198.0 | 11.0 | 11.5 | 10.7 |
| 10 | $z = 1$–$2$ $L_X = 10^{42-44}$ $N_H < 10^{23}$ | 51 | 4 | 47 | 1.38 | 1.18 | 1.40 | 43.36 | 43.60 | 43.34 | 920 ± 110 | 6190 ± 320 | 470 ± 120 | 208.1 | 818.5 | 156.2 | 11.5 | 12.3 | 11.2 |
| 11 | $z = 0.5$–$1$ $L_X = 10^{42-43}$ $N_H < 10^{23}$ | 44 | 3 | 41 | 0.74 | 0.58 | 0.75 | 42.63 | 42.65 | 42.63 | 1390 ± 130 | 12 850 ± 820 | 550 ± 130 | 167.8 | 688.3 | 129.7 | 11.0 | 11.4 | 10.7 |
| 12 | $z = 1$–$2$ $L_X = 10^{42-43}$ $N_H < 10^{23}$ | 19 | 1 | 18 | 1.35 | 1.03 | 1.37 | 42.68 | 42.49 | 42.69 | 1110 ± 170 | 8150 ± 750 | 720 ± 170 | 153.0 | 555.6 | 130.6 | 11.7 | 11.9 | 11.4 |
| 13 | $z = 0.5$–$1$ $L_X = 10^{43-44}$ $N_H < 10^{23}$ | 19 | 3 | 16 | 0.77 | 0.81 | 0.76 | 43.43 | 43.28 | 43.46 | 1510 ± 200 | 6060 ± 410 | 660 ± 230 | 413.1 | 625.9 | 373.2 | 11.1 | 11.8 | <11.2 |
| 14 | $z = 1$–$2$ $L_X = 10^{43-44}$ $N_H < 10^{23}$ | 32 | 3 | 29 | 1.40 | 1.23 | 1.42 | 43.53 | 43.72 | 43.51 | 870 ± 140 | 5540 ± 340 | 390 ± 150 | 240.9 | 906.1 | 172.1 | 11.5 | 12.3 | <11.7 |
| 15 | $S_{24} = 50$–$150$ μJy | 68 | 0 | 68 | 1.40 | – | 1.40 | 43.73 | – | 43.73 | 260 ± 90 | – | 260 ± 90 | 113.2 | – | 113.2 | <11.4 | – | <11.4 |
| 16 | $S_{24} = 150$–$500$ μJy | 68 | 10 | 58 | 1.37 | 1.00 | 1.44 | 43.75 | 43.52 | 43.78 | 1263 ± 97 | 4420 ± 180 | 720 ± 110 | 285.9 | 456.9 | 256.4 | 11.7 | 11.9 | 11.5 |
| 17 | $S_{24} \geq 500$ μJy | 20 | 13 | 7 | 1.10 | 1.01 | 1.27 | 44.02 | 44.01 | 44.04 | 7040 ± 230 | 10 120 ± 300 | 1330 ± 320 | 1113.4 | 1199.7 | 953.0 | 12.2 | 12.3 | 11.6 |
| 18 | $S_{24} \geq 50$ μJy | 156 | 23 | 133 | 1.35 | 1.01 | 1.41 | 43.79 | 43.86 | 43.77 | 1570 ± 66 | 7640 ± 190 | 520 ± 70 | 316.7 | 876.8 | 219.9 | 11.7 | 12.1 | 11.3 |

*Notes.* (1) Stack index; (2) stack description; (3) the numbers of CDF-S AGNs/SBs in each stack; (4) mean redshift of the sources in each stack; (5) logarithm of the mean, absorption corrected X-ray luminosity of the sources in each stack; (7) stacked 70 μm flux density per source; and (8) stacked 24 μm flux density per source; and (9) IR luminosity per source (over the 8–1000 μm interval), derived from the 70 μm flux density. Upper limits include the uncertainty on the $S_{70} - L_{IR}$ correction. We do not calculate $L_{IR}$ for stack (4), $z > 3$ AGN, as the mean redshift is beyond the range of the tracks derived from the BAT/IRS sample.

$L_X = 10^{42-43}$ and $10^{43-44}$ erg s$^{-1}$ bins. However, the conservative upper limits on the $S_{70}/S_{24}$ flux ratios of the $L_X = 10^{43-44}$ erg s$^{-1}$ 70 μm *undetected* AGNs place them below those of the $L_X = 10^{42-43}$ erg s$^{-1}$ 70 μm *undetected* AGNs in each redshift bin. Based on the BAT/IRS tracks, this result suggests that the more X-ray luminous AGNs may have, on average, more AGN-dominated IR SEDs than their lower $L_X$ counterparts; however, deeper data will be required to confirm this result. However, we find that the stacks of the $L_X = 10^{42-43}$ erg s$^{-1}$ AGNs lie in ambiguous regions of the $S_{70}/S_{24} - z$ plot, which limits the conclusions that can be directly derived on the relative contributions from AGN and SB activity to these stacks using the $S_{70}/S_{24}$ flux ratios alone; in Section 4.1, we explore a variety of approaches to constrain the relative AGN and SB contributions using additional data.

### 3.2.2 Average IR fluxes and luminosities

The average IR luminosities of the stacked subsamples are calculated by taking the same approach as that used for the individual 70 μm detected sources (see Section 3.1.3). For those stacks with less than 3σ detections, we use the nominal $S_{70}/S_{24}$ flux ratio (rather than upper limits) when determining the closest match out of the five tracks considered; although, we note that using upper limits to select the appropriate track changes the estimates of $L_{IR}$ by less than 20 per cent. In both redshift bins, the nominal $S_{70}/S_{24}$ flux ratios of the $L_X = 10^{42-43}$ and $10^{43-44}$ erg s$^{-1}$ 70 μm *undetected* stacks are most closely matched by the average AGN and average QSO SEDs, respectively. We note, however, that the 3σ upper limits on the $S_{70}/S_{24}$ flux ratios of stacked $L_X = 10^{43-44}$ erg s$^{-1}$ AGNs are also consistent with the average AGN SED (see Fig. 4).

In Fig. 5, we plot the IR luminosity versus $L_X$ for the CDF-S X-ray sources and the BAT/*IRAS* sample. In the case of the $L_X = 10^{42-43}$ erg s$^{-1}$ *undetected* AGNs, we find that $L_{IR}$ is larger by a factor of ≈5 for the $z = 1.0$–2.0 AGNs when compared to the $z = 0.5$–1.0 AGNs ($L_{IR} = 2.5 \times 10^{11}$ and $5.0 \times 10^{10}$ L$_\odot$, respectively), and a factor of ≈20 times larger than the average $42 < \log(L_X/$ erg s$^{-1}) < 43$, $N_H < 10^{23}$ cm$^{-2}$ BAT/IRS AGN (i.e. at $z \approx 0$; $L_{IR} = 1.3 \times 10^{10}$ L$_\odot$). This is in spite of these subsamples having almost the same average X-ray luminosities ($\overline{L_X} = 4.9 \times 10^{42}$, $4.3 \times 10^{42}$ and $3.7 \times 10^{42}$ erg s$^{-1}$ for $z = 1.0$–2.0, 0.5–1.0 and $z \approx 0$ AGNs, respectively). This difference corresponds to a factor of $4.7^{+10.2}_{-2.0}$ and $12.7^{+7.1}_{-2.6}$ increase in $L_{IR}/L_X$ from $z = 0.5$–1 to 1–2 and from $z \approx 0$ to 1.0–2.0, respectively (these conservative errors correspond to the full range of IR luminosities derived using all five tracks in Fig. 4). The stacked data, therefore, suggest that the average $L_{IR}/L_X$ ratio of $L_X = 10^{42-43}$ erg s$^{-1}$ AGNs strongly evolves with redshift, as illustrated in Fig. 6. Although this result is based on stacking analyses, we show in Section 3.3 that we obtain the same result using 24 μm constraints for individual sources.

The 70 μm *undetected* stacks of the $L_X = 10^{43-44}$ erg s$^{-1}$ AGNs at both $z = 0.5$–1 and 1–2 are not significantly detected, limiting the constraints that we can place on $L_{IR}$ using the 70 μm data alone; the limits are $L_{IR} < 1.5 \times 10^{11}$ and $<4.6 \times 10^{11}$ L$_\odot$ for the AGNs at $z = 0.5$–1 and 1–2, respectively (these upper limits include the uncertainty in the $S_{70} - L_{IR}$ correction). However, because the upper limits on the $S_{70}/S_{24}$ flux ratios of these stacks provide significant constraints to the range of potential matching BAT/IRS AGN SEDs, we can estimate the average IR luminosities from the stacked 24 μm flux densities to a much higher degree of accuracy than would normally be the case (to within a factor of ≈3, rather than ≈12). This reduced uncertainty is based on the fact that the $S_{70}/S_{24}$ flux
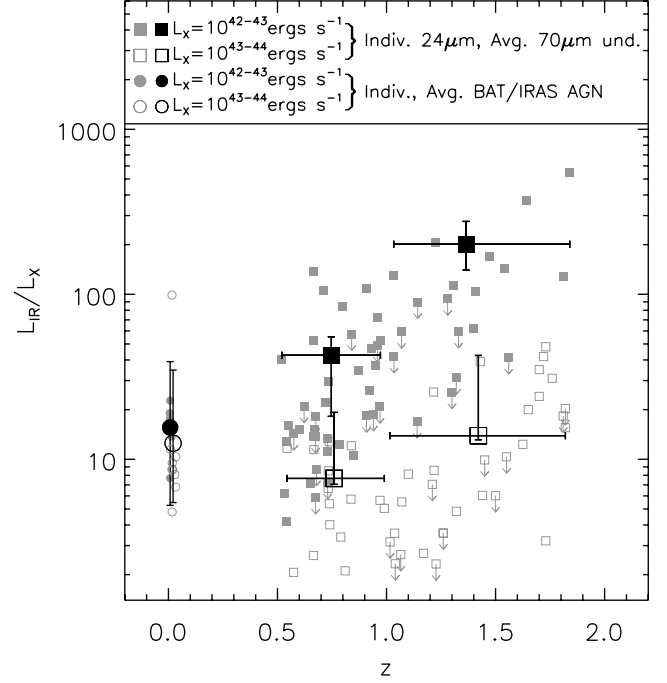


**Figure 6.** $L_{IR}/L_X$ versus redshift for the stacked 70 μm *undetected* sources in the 'Restricted' sample of CDF-S X-ray AGNs, separated according to $L_X$ (black squares). Vertical error bars indicate the range of $L_{IR}/L_X$ produced by assuming the various tracks in Figs 3 and 4. Small, grey squares indicate the $L_{IR}/L_X$ ratios of each X-ray AGN in the 'Restricted' sample derived from their 24 μm flux densities, assuming the average AGN and average QSO SEDs for the $L_X = 10^{42-43}$ and $L_X = 10^{43-44}$ erg s$^{-1}$ AGNs, respectively (see Section 3.3). For those sources undetected at 24 μm, we derive upper limits by assuming a 24 μm flux density limit of 50 μJy. For comparison, we include the individual and average $L_{IR}/L_X$ ratios of the BAT/*IRAS* sample, separated according to $L_X$ (vertical error bars indicate the standard deviation of $L_{IR}/L_X$ of the BAT/IRS sample). Both the stacking analysis and the individual 24 μm detections clearly show a consistent increase in the $L_{IR}/L_X$ ratio of $L_X = 10^{42-43}$ erg s$^{-1}$ AGN from $z \approx 0$ to $z = 1$–2.

ratios of the $L_X = 10^{43-44}$ erg s$^{-1}$ AGN stacks restricts us to AGN-dominated BAT/IRS SEDs, which all have similar $S_{24} - L_{IR}$ ratios. Using the stacked 24 μm flux density, we obtain $L_{IR} = 5.6 \times 10^{10}$ and $1.2 \times 10^{11}$ L$_\odot$ for the $L_X = 10^{43-44}$ erg s$^{-1}$ AGNs in the $z = 0.5$–1.0 and 1.0–2.0 redshift bins, respectively, corresponding to a factor of ≈2 increase between these redshift ranges. For comparison, the average $L_{IR}$ of $L_X = 10^{43-44}$ erg s$^{-1}$ AGNs in the $z \approx 0$ BAT/IRS sample is $1.2 \times 10^{11}$ L$_\odot$. Given the average X-ray luminosities of these AGNs ($\overline{L_X} = 3.8 \times 10^{43}$, $2.9 \times 10^{43}$ and $3.2 \times 10^{43}$ erg s$^{-1}$ for the $z \approx 0$, $z = 0.5$–1 and $z = 1$–2 AGNs, respectively), we constrain the change in $L_{IR}/L_X$ to a factor of $\approx 1.8^{+4.2}_{-1.0}$ between $z = 0.5$–1 and 1–2 and to a factor of $\approx 1.2^{+2.6}_{-0.8}$ between $z \approx 0$ and 1–2, both of which are consistent with no evolution (see Fig. 6).

A number of recent studies have shown that the MIR emission of AGNs can be used as a good proxy for their intrinsic luminosities (e.g. Krabbe, Böker & Maiolino 2001; Lutz et al. 2004; Maiolino et al. 2007; Horst et al. 2008). Understanding how the X-ray–MIR relationship changes with redshift would be very useful for detecting potentially heavily obscured AGNs (e.g. Daddi et al. 2007; Fiore et al. 2008; Georgantopoulos et al. 2008). However, previous X-ray–MIR studies of AGNs have been limited to extremely high-luminosity sources (i.e. $\overline{L_X} = 3 \times 10^{45}$ erg s$^{-1}$) at redshifts beyond $z \approx 0.3$. Using the results from our stacking analyses, we can

**Table 3.** Average properties of the CDF-S X-ray AGNs in the 70 μm *undetected*, 'Restricted' sample (see Section 2.1.1).

| | | | | | Stacks | | Avg. AGN/QSO | | BAT/*IRAS* closest match | |
|---|---|---|---|---|---|---|---|---|---|---|
| | $N_{\rm all}$ | $N_{\rm det}$ | $\overline{z}$ | $\log(\overline{L_{\rm X}})$ | $\log(\widetilde{L_{\rm X}})$ | $\frac{\overline{L_{\rm IR,70}}}{L_{\rm X}}$ | $\frac{\overline{L_{\rm IR,24}}}{L_{\rm X}}$ | $\frac{\overline{L_{\rm IR,24}}}{L_{\rm X}}$ | $\frac{\widetilde{L_{\rm IR,24}}}{L_{\rm X}}$ | $\frac{\overline{L_{\rm IR,24}}}{L_{\rm X}}$ | $\frac{\widetilde{L_{\rm IR,24}}}{L_{\rm X}}$ |
| $z = 0.5$–1, $L_{\rm X} = 10^{42-43}$ erg s$^{-1}$ | 41 | 28 | 0.7 | 42.6 | 42.6 | 42.7 | 26.2 | 24.9 | 18.0 | 28.1 | 20.3 |
| $z = 1$–2, $L_{\rm X} = 10^{42-43}$ erg s$^{-1}$ | 19 | 10 | 1.4 | 42.7 | 42.6 | 201.2 | 133.3 | 112.6 | 80.2 | 164.2 | 100.2 |
| $z = 0.5$–1, $L_{\rm X} = 10^{43-44}$ erg s$^{-1}$ | 16 | 15 | 0.8 | 43.5 | 43.4 | < 17.4 | 7.7 | 6.4 | 5.3 | 8.9 | 7.7 |
| $z = 1$–2, $L_{\rm X} = 10^{43-44}$ erg s$^{-1}$ | 30 | 19 | 1.4 | 43.5 | 43.4 | < 35.1 | 13.9 | 11.4 | 7.8 | 19.9 | 14.1 |

*Note.* $N_{\rm all}$ is the number of AGNs detected in each bin and $N_{\rm det}$ is the number of these that are detected at 24 μm. $\overline{z}$ is the mean redshift of the AGNs in each subsample and $\log(\overline{L_{\rm X}})$ and $\log(\widetilde{L_{\rm X}})$ indicate their mean and median $L_{\rm X}$. We provide the mean $L_{\rm IR}/L_{\rm X}$ ratios derived from the 70 and 24 μm stacks (assuming the average AGN and average QSO SEDs for the $L_{\rm X} = 10^{42-43}$ and $10^{43-44}$ erg s$^{-1}$ subsamples, respectively) as well as the mean and median $L_{\rm IR}/L_{\rm X}$ ratios derived from the individual 24 μm flux densities. Finally, we provide the mean and median $L_{\rm IR}/L_{\rm X}$ derived from the individual 24 μm flux densities assuming the two BAT/*IRAS* tracks that most closely match the $S_{70}/S_{24}$ flux ratios of the $L_{\rm X} = 10^{42-43}$ and $10^{43-44}$ erg s$^{-1}$ subsamples at both $z = 0.5 - 1$ and 1–2: NGC 1275 and Mrk 290, respectively.

constrain the X-ray–MIR luminosity ratios [hereafter we focus on $\nu L_\nu (6\,\mu$ m$)/L_{\rm X}$] of more typical, distant AGNs found in deep, multiwavelength surveys. At $z \approx 0$, the $\nu L_\nu (6\,\mu$ m$)/L_{\rm X}$ ratios of the average AGN and average QSO SEDs are consistent with Lutz et al. (2004) (i.e. $\approx$3 and $\approx$2, respectively).[7] To calculate the $\nu L_\nu (6\,\mu$m$)/L_{\rm X}$ ratios of the CDF-S AGNs we assume the same SEDs as those used to derive their $L_{\rm IR}/L_{\rm X}$ ratios (i.e. average AGN and average QSO for $L_{\rm X} = 10^{42-43}$ erg s$^{-1}$ and $L_{\rm X} = 10^{43-44}$ erg s$^{-1}$ AGNs, respectively). We, therefore, find that the average $\nu L_\nu (6\,\mu$m$)/L_{\rm X}$ ratios of $L_{\rm X} = 10^{42-43}$ erg s$^{-1}$ AGNs increase from $\approx$3 at $z \approx 0$ to $\approx$10 and $\approx$43 at $z = 0.5$–1 and 1–2, respectively. By contrast, the average $\nu L_\nu (6\,\mu$m$)/L_{\rm X}$ ratios of $L_{\rm X} = 10^{43-44}$ erg s$^{-1}$ AGNs remain largely unchanged to $z \approx 2$ [i.e. $\nu L_\nu (6\,\mu$m$)/L_{\rm X} \approx 1$–2]. Our data, therefore, suggest that deep IR observations can be used as a reliable method of identifying intrinsically bright (i.e. $L_{\rm X} = 10^{43-44}$ erg s$^{-1}$), potentially Compton-thick AGNs. However, we urge caution when using either the $L_{\rm IR}/L_{\rm X}$ or $\nu L_\nu (6\,\mu$m$)/L_{\rm X}$ ratios to locate less luminous obscured AGNs (i.e. $L_{\rm X} \lesssim 10^{43}$ erg s$^{-1}$) unless other indicators of luminous AGN activity are present (e.g. emission line spectra; see Alexander et al. 2008).

### 3.3 24 μm properties

The results on the $L_{\rm IR}/L_{\rm X}$ ratios in Section 3.2 were based on stacking analyses, which could be biased by a few bright 70 μm undetected sources. Since the majority of the CDF-S X-ray AGNs are individually detected at 24 μm, we can perform a complementary test of our results that does not rely significantly on stacking analyses. The advantage of this approach is that we can assess the range of $L_{\rm IR}$ for the X-ray AGNs, although there can be considerable uncertainty in the conversion between 24 μm flux density and $L_{\rm IR}$ for individual objects (see Fig. 3). However, as we show in Fig. 3, provided the average SED is not predominantly SB-dominated, then we can predict the average $L_{\rm IR}/L_{\rm X}$ ratio, on the basis of the 24 μm data, to within a factor of $\approx$3; on the basis of Fig. 4, the average SEDs are AGN-dominated, and would be increasingly so if the stacked 70 μm flux is dominated by bright undetected sources. Furthermore, so long as the average SEDs of the $z = 0.5$–1 AGNs are the same

as the $z= 1$–2 AGNs, then we can accurately assess the relative change in $L_{\rm IR}/L_{\rm X}$ between these redshifts; we provide evidence in Section 4.1 that this does appear to be the case. To convert from 24 μm flux densities to $L_{\rm IR}$, we use the same SEDs as assumed when calculating $L_{\rm IR}$ from the stacked 70 μm flux densities (i.e. average AGN and average QSO for the $L_{\rm X} = 10^{42-43}$ and $10^{43-44}$ erg s$^{-1}$ AGNs, respectively; see Section 3.2.2). For those AGNs that are undetected at 24 μm, we calculated upper limits on $L_{\rm IR}$ assuming $S_{24} = 50$ μJy; however, we note that this assumption has a small effect on our average results (i.e. $\overline{L_{\rm IR}/L_{\rm X}}$ only changes by $\approx$35 per cent even if we assume extreme upper limits of $S_{24} = 0$ μJy). The average $L_{\rm IR}/L_{\rm X}$ ratios derived from the 24 μm fluxes are given in Table 1.

In Fig. 6, we include the individual $L_{\rm IR}/L_{\rm X}$ ratios calculated using the $L_{\rm IR}$ values derived from 24 μm fluxes of the 70 μm *undetected* AGNs in the 'Restricted' sample. For both the $L_{\rm X} = 10^{42-43}$ and $L_{\rm X} = 10^{43-44}$ erg s$^{-1}$ AGNs, the mean $L_{\rm IR}/L_{\rm X}$ ratios increase with redshift by factors of $\approx$4.5 and $\approx$1.8, respectively. These results are in qualitative agreement with those obtained from the 70 μm stacks and indicates that the stacks are not dominated by a few extreme sources; these results are also confirmed by the median $L_{\rm IR}/L_{\rm X}$ ratios presented in Table 3. However, we note that there is a factor of $\approx$2 offset between the $L_{\rm IR}/L_{\rm X}$ ratios derived from the 70 μm stacks and individual 24 μm flux densities. This is caused by the difference between the $S_{70}/S_{24}$ flux ratios of the 70 μm *undetected* stacks and the assumed SEDs (see Fig. 4) and disappears if we assume the SEDs of the two individual BAT/IRS AGNs that most closely reproduce (at both redshift bins) the $S_{70}/S_{24}$ flux ratios of the 70 μm *undetected* $L_{\rm X} = 10^{42-43}$ and $10^{43-44}$ erg s$^{-1}$ stacks: NGC 1275 and Mrk 290, respectively.

### 4 DISCUSSION

We have provided multiple lines of evidence for an increase in the $L_{\rm IR}/L_{\rm X}$ ratio for AGNs over the redshift range $z = 0$–2, with $L_{\rm X} = 10^{42-43}$ erg s$^{-1}$ AGNs $\approx$5 times more IR luminous at $z = 1$–2 than at $z = 0.5$–1 (and $\approx$20 times more IR luminous than at $z \approx 0$). The evidence for an increase in $L_{\rm IR}$ for $L_{\rm X} = 10^{43-44}$ erg s$^{-1}$ AGNs is less conclusive: a factor of $\approx$2 between $z = 0.5$–1 and 1–2 and no change from $z \approx 0$ and 1–2.

These results provide new insight into the production of IR emission from distant AGNs and lead to a number of questions, which we address below.

---

[7] We also note that the $\nu L_\nu (10.5\,\mu$m$)/L_{\rm X}$ ratios of the average AGN and average QSO at $z \approx 0$ are largely consistent with the relationship presented in Krabbe et al. (2001) [i.e. $\nu L_\nu (10.5\,\mu$m$)/L_{\rm X} \approx 2.5$ and $\approx$1.9, respectively].

### 4.1 What is driving the increase in $L_{IR}$?

The $L_{IR}/L_X$ ratio for the $L_X = 10^{42-43}$ erg s$^{-1}$ AGNs at $z = 1$–2 is higher than that found for lower redshift X-ray AGNs (see Table 3). However, the $L_{IR}/L_X$ ratio for the $L_X = 10^{42-43}$ erg s$^{-1}$ AGNs is broadly consistent with $z \approx 2$ submillimeter emitting galaxies (SMGs) hosting AGN activity ($L_{FIR}/L_X \approx 250$; Alexander et al. 2005). On the basis of sensitive *Spitzer*-IRS spectroscopy, the large $L_{FIR}/L_X$ ratio from AGN-hosting SMGs appears to be due to intense star formation activity, with an average contribution to $L_{FIR}$ from AGN activity of $\approx 10$ per cent (e.g. Pope et al. 2008; Menéndez-Delmestre et al. 2007, 2009). Can the increase in the average $L_{IR}/L_X$ ratio of the $z = 1$–2 AGNs also be due to increased star formation activity?

There is no clear relative offset between the stacked $S_{70}/S_{24}$ flux ratio and the AGN-dominated track for the $L_X = 10^{42-43}$ erg s$^{-1}$ AGNs over the redshift range $z = 0.5$–2, appearing to suggest that the relative AGN/SB contribution to $L_{IR}$ has not changed with redshift. If we derive the relative AGN/SB contribution to the stacked $S_{70}/S_{24}$ using the average AGN and SB tracks, then we estimate $\approx 60$ and $\approx 70$ per cent of the AGNs with $L_X = 10^{42-43}$ erg s$^{-1}$ have AGN-dominated SEDs at $z = 0.5$–1 and 1–2, respectively; by comparison, the stacked $S_{70}/S_{24}$ of the $L_X = 10^{43-44}$ erg s$^{-1}$ AGNs suggest $\approx 100$ per cent have AGN-dominated SEDs over the full redshift range. However, since it is difficult to unambiguously determine the relative AGN/SB contribution to $L_{IR}$ from the $S_{70}/S_{24}$ flux ratios at $z > 1.5$ (see Fig. 4), this result should be considered tentative.[8] Therefore, we explore below the implication of our results assuming both an increase in star formation and AGN activity.

If the observed increase in $L_{IR}$ is attributed to star formation, it would imply a significantly higher (i.e. a factor of $\approx 5$) ratio between star formation and black hole growth at $z = 1$–2 compared to $z = 0.5$–1, and a factor of $\approx 13$ increase between $z \approx 0$ and 1–2. Whether this has significant implications for the black hole–bulge mass relationship depends on the location of the star formation in the host galaxy and on the AGN fraction (i.e. the duty cycle of black hole growth). For example, using equation (4) of Kennicutt (1998) to derive the star formation rate from $L_{IR}$ and deriving the mass accretion rate from $L_X$, we estimate that the ratio between the average star formation and mass accretion rate is $\approx 500$ in the $z = 1$–2 AGNs, which is consistent with the black hole to bulge mass ratio observed in the local Universe (i.e. $\approx 800$; McLure & Dunlop 2002; Marconi & Hunt 2003). This would appear to suggest a closer relationship between black hole and stellar growth at $z = 1$–2 than found at $z = 0.5$–1, where the average star formation and mass accretion rate would be $\approx 100$ (and $\approx 30$ at $z \approx 0$), based on the same assumptions as above. However, these different results could be reconciled if the AGN fraction is higher at higher redshifts or if the majority of the star formation at higher redshifts is occurring in the galaxy disc rather than the galaxy bulge, or vice versa.

If, however, the increase in the $L_{IR}/L_X$ ratio is due to the AGN, it would imply that a larger fraction of the intrinsic emission from the accretion disc is reprocessed by dust. This increase in the $L_{IR}/L_X$ ratio may, therefore, be due to larger AGN dust covering factors at

---

[8] We note that we also find a similar fraction ($\approx 30$ per cent) of $L_X = 10^{42-43}$ erg s$^{-1}$ AGNs at $z = 1$–2 have IRAC 3.6–8.0 $\mu$m colours suggesting AGN-dominated SEDs (based on Stern et al. 2005) as that found for $L_X = 10^{42-43}$ erg s$^{-1}$ AGNs at $z = 0.5$–1. This also suggests that the relative AGN/SB contribution for $L_X = 10^{42-43}$ erg s$^{-1}$ AGNs is constant with redshift but we caution that this result is based on shorter wavelength data than used to derive $L_{IR}$.

higher redshifts; there is tentative evidence that this is indeed the case from measurements of the obscured to unobscured ratios of AGNs in deep X-ray surveys (e.g. La Franca et al. 2005; Hasinger 2008). Results presented in Hasinger (2008) predict a factor of $\approx 2$ increase in the ratio of obscured-to-unobscured AGNs between $z = 0$ and 1–2, significantly lower than what we measure here. However, this is based on a sample of AGNs covering a broader range of $L_X$ than focused on here and there is evidence that any increase in the dust covering fraction will be weaker in more X-ray luminous AGNs (e.g. Ueda et al. 2003; Akylas et al. 2006; Treister, Krolik & Dullemond 2008; and supported by the reduced $L_{IR}/L_X$ ratios of the $L_X = 10^{43-44}$ erg s$^{-1}$ AGNs reported here). Therefore, on the basis of the X-ray survey results, it is plausible that at least some of the increase in $L_{IR}/L_X$ ratio is due to a larger dust covering factor at $z \approx 1$–2 than seen at lower redshifts. An increase in dust-covering factor with redshift is predicted by a number of theoretical models, which suggest that AGNs undergo early growth during a hidden phase before expelling their obscuring gas and dust, revealing a luminous, unobscured quasar (Silk & Rees 1998; Springel, Di Matteo & Hernquist 2005; Hopkins et al. 2006).

More direct constraints on the origin of the increase in the $L_{IR}/L_X$ ratio will be placed using the *Herschel Space Observatory* (see Section 4.3) and *Spitzer*-IRS, for the fraction of X-ray AGNs that have *Spitzer*-IRS data (see Mullaney et al., in preparation).
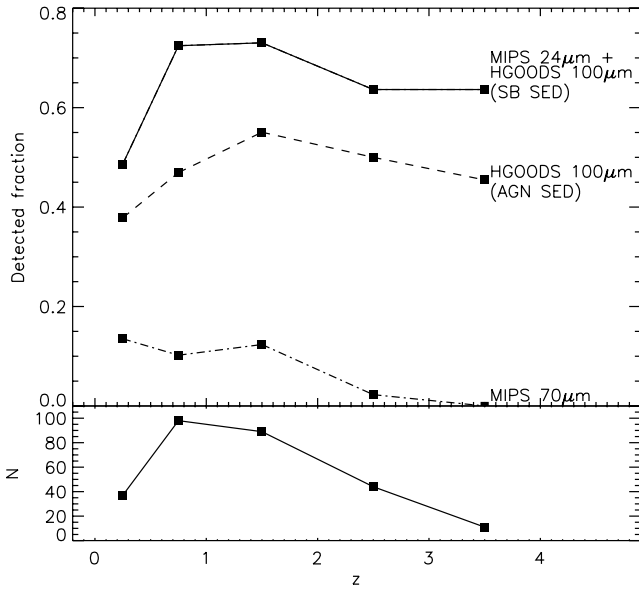
### 4.2 What is the contribution of AGNs to the cosmic IR background?

We can use the results of our stacking analysis to place constraints on the AGN contribution to the 70 $\mu$m background. If we stack all of the 251 X-ray AGNs, irrespective of whether they are individually detected at 70 $\mu$m, we obtain an average 70 $\mu$m flux density of $1040 \pm 80$ $\mu$Jy, and therefore an integrated 70 $\mu$m flux density of $260 \pm 20$ mJy, over the 391.3 arcmin$^2$ of the CDF-S field. On the basis of the analysis of the IR background in both GOODS fields and the Lockman Hole (e.g. Dole et al. 2006), this corresponds to $\gtrsim 5$ per cent of the average resolved 70 $\mu$m background. This constraint is a lower limit since (i) the X-ray observations will not have identified the most heavily obscured luminous AGNs in this field, (ii) the 70 $\mu$m field is too small to include X-ray bright AGNs and (iii) the X-ray observations are not sensitive to the lowest luminosity AGNs.

On the basis of Tozzi et al. (2006), we would predict $\approx 80$ per cent of $L_X > 10^{41}$ erg s$^{-1}$, $N_H < 10^{23}$ AGNs in the CDF-S (i.e. to $z \approx 5$) to be X-ray undetected. If we assume that they have the same IR SED as the X-ray detected AGNs, then they increase our estimate of the resolved 70 $\mu$m background by a factor of 5 to $\gtrsim 25$ per cent; from a study of nearby sources, Lutz et al. (2004) finds that the IR emission of AGNs is not significantly depressed in the most heavily obscured sources (we confirm that this is also the case for the BAT/IRS sample). Since X-ray surveys are insensitive to the most heavily obscured AGNs (i.e. Compton-thick sources with $N_H > 10^{24}$ cm$^{-2}$), the overall contribution to the 70 $\mu$m background could potentially double to $\gtrsim 10$ per cent (e.g. Daddi et al. 2007; Alexander et al. 2008).

To estimate the contribution to the 70 $\mu$m background from bright AGNs that are too rare to lie in the small CDF-S field would require the same analyses as performed here to be made on a shallower survey that covers a larger area of the sky. As it stands, the most accurate 70 $\mu$m analysis in a larger field is that of Papovich et al. (2007) of the E-CDFS. They find that bright AGNs (i.e. $L_X > 10^{44}$ erg s$^{-1}$) contribute only $7 \times 10^{-4}$ MJy sr$^{-1}$ to the IR background at 70 $\mu$m, corresponding to an insignificant fraction

**Figure 7.** Top: predicted fractions of CDF-S X-ray AGNs detected in the upcoming HGOODS deep IR survey to be undertaken by the *Herschel Space Observatory*. The expected observed 100 μm flux densities are calculated by extrapolating the *Spitzer*-MIPS 24 μm flux densities along the average SB-dominated and average AGN-dominated SEDs, derived from the BAT/IRS sample of AGNs. If all the X-ray AGNs were to have SB-dominated IR SEDs, we would expect to detect *at least* as high a fraction at 100 μm as we currently detect at 24 μm. Also shown for comparison are the fractions of CDF-S AGNs detected by MIPS at 70 μm in each redshift bin. Bottom: the number of CDF-S X-ray AGNs in each redshift bin.

(≪1 per cent) of the total IR background at this wavelength. However, the E-CDFS field is not a great deal larger than the CDF-S field and a full study of the contribution of X-ray bright AGNs to the IR background will require the analysis of the much larger Cosmological Evolution Survey (COSMOS)[9] and/or Bootes[10] fields at 70 μm.

### 4.3 What advances may we expect for deep surveys with *Herschel*?

Our study of the FIR properties of X-ray detected AGNs allows us to place constraints on the properties of AGNs detected in deep *Herschel* fields at >70 μm. We anticipate that the improved sensitivity of *Herschel*'s Photometer Array Camera (PACS)† over *Spitzer*-MIPS will result in a significant increase in the fractions of X-ray AGNs that will be detected at FIR wavelengths, which will provide more direct insight into the processes driving the increase in $L_{IR}$ at $z = 1$–2. Depending on the assumed SED, we predict that approximately 45–60, 50–70, 50–65 and 45–65 per cent of the CDF-S X-ray sources at $z < 1$, $z = 1$–2, 2–3 and 3–4, respectively, will be detected at 100 μm in the proposed ultradeep HGOODS survey (limiting flux = 0.6 mJy; see Fig. 7). These estimated detection levels are calculated by extrapolating the 24 μm flux densities along the average SB-dominated and average AGN-dominated SEDs (derived from the BAT/IRS sample).

In Fig. 8, we present the results of passing the IR spectra of the BAT/IRS sample through the various PACS filter response curves. Our analysis shows that, although the $S_{100}/S_{24}$ flux ratio will not
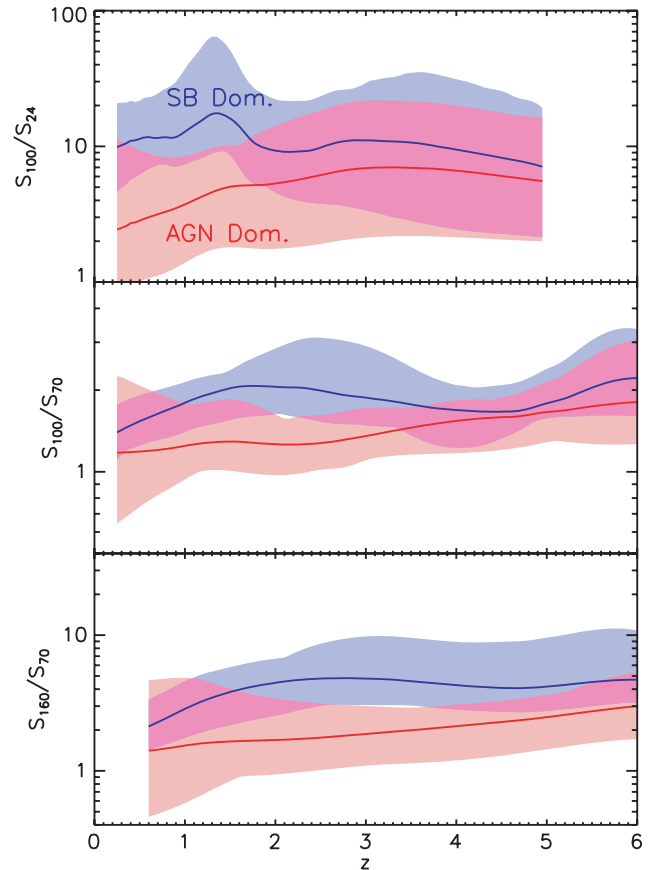
**Figure 8.** AGN/SB diagnostic powers of the PACS filters on board *Herschel Space Observatory*. The shaded regions indicate the range of expected infrared flux ratios of the AGNs in the BAT/IRS sample at the redshifts shown. Solid lines indicate the expected infrared flux ratios of the BAT/IRS average AGN and average SB.

push our constraints on the relative contributions from AGN activity and star formation to higher redshifts (due to the influence of the MIR spectral features that shift into the observed 24 μm band at high redshifts), the $S_{100}/S_{70}$ and $S_{160}/S_{70}$ flux ratios will 'take over' and provide this information out to a redshift of ∼5 (i.e. the redshift of the most distant AGNs currently detected in the deepest X-ray surveys). Deep, IR observations undertaken by *Herschel* will, therefore, provide a method of identifying a significant proportion of the long sought after population of Compton-thick AGNs out to $z \approx 6$.

## 5 SUMMARY

We have investigated the MIR and FIR properties of X-ray detected AGNs and SBs in the CDF-S using deep 24 and 70 μm observations undertaken by the *Spitzer Space Telescope* as part of the GOODS and FIDEL legacy surveys. Out of the 266 X-ray AGNs/SBs, 30 (≈11 per cent) and 172 (≈65 per cent) have counterparts at 70 and 24 μm, respectively, with a bias towards the detection of SBs and BLAGNs at 70 μm. As the majority of CDF-S X-ray AGNs are undetected at 70 μm, we rely on stacking analysis to measure their average MIR and FIR properties. We compare the IR properties of the CDF-S AGNs/SBs with those of a sample of local AGNs that have X-ray properties (i.e. $L_X$ and $N_H$) covering the same range as the CDF-S AGNs (i.e. the BAT/IRS sample). In the following points, we summarize the main conclusions of this study:

(i) We find strong evidence at both 24 and 70 μm that the average IR luminosity of $L_X = 10^{42-43}$ erg s$^{-1}$ AGNs at $z = 1-2$ is significantly higher than those at $z = 0.5-1$ and $z \approx 0$ (i.e. by a factor of $\approx 5$ and $\approx 20$, respectively). This difference corresponds to a factor of $4.7^{+10.2}_{-2.0}$ and $12.7^{+7.1}_{-2.6}$ increase in $L_{IR}/L_X$, respectively. This large increase in $L_{IR}$ is not, however, seen for AGNs with higher X-ray luminosities (i.e. $L_X = 10^{43-44}$ erg s$^{-1}$). We, therefore, argue that deep IR observations can be used as a reliable method to identify intrinsically bright (i.e. $L_X = 10^{43-44}$ erg s$^{-1}$) Compton-thick AGNs, but urge caution when using this ratio to locate less luminous obscured AGNs (i.e. $L_X \lesssim 10^{43}$ erg s$^{-1}$), unless other indicators of AGN activity are present.

(ii) Due to the low numbers of AGNs detected at 70 μm, we are unable to establish what process is driving this increase in the average $L_{IR}$; however, both increased star formation and/or increased AGN dust covering factors are likely candidates. If the former, then the $z = 1-2$ epoch may represent a period of rapid growth of the bulge to black hole mass ratio. However, there is tentative evidence from X-ray observations that the dust covering fraction is, indeed, higher at large redshifts. We predict that the forthcoming deep surveys to be carried out by the *Herschel Space Observatory* will enable us to resolve what process is driving the increase in $L_{IR}$ (see Sections 3.2.2, 3.3 and 4.1).

(iii) On average, more X-ray luminous CDF-S AGNs have lower $S_{70}/S_{24}$ flux ratios. Based on the IR properties of a sample of local AGNs with similar X-ray properties (i.e. $L_X$ and $N_H$), we conclude that more X-ray luminous CDF-S AGNs have IR SEDs that are more AGN-dominated (rather than SB-dominated) (see Section 3.2.1).

(iv) Despite measuring a large increase in $L_{IR}$ among $z = 1-2$ AGNs [see point (i) above], we find that the X-ray detected AGNs in the CDF-S contribute only $\approx 5$ per cent of the 70 μm background. However, if we extrapolate this fraction to take into account those $\approx 80$ per cent of AGNs that are undetected in X-rays, we estimate that $\approx 25$ per cent of the 70 μm background is attributable to AGNs (see Section 4.2).

(v) We anticipate that the undertaking of deep, FIR surveys by the *Herschel Space Observatory* will allow us to detect between 40 and 75 per cent of the X-ray detected AGNs in the 1 Ms CDF-S, depending on whether the IR SEDs are predominantly AGN- or SB-dominated, respectively. Furthermore, the FIR diagnostics used in our analysis can be directly applied to the PACS filters on board *Herschel* to enable us to discriminate between AGNs with SB- or AGN-dominated IR SEDs (see Section 4.3).

## REFERENCES

Akylas A., Georgantopoulos I., Georgakakis A., Kitsionas S., Hatziminaoglou E., 2006, A&A, 459, 693

Alexander D. M., Brandt W. N., Hornschemeier A. E., Garmire G. P., Schneider D. P., Bauer F. E., Griffiths R. E., 2001, AJ, 122, 2156

Alexander D. M. et al., 2003, AJ, 126, 539

Alexander D. M., Bauer F. E., Chapman S. C., Smail I., Blain A. W., Brandt W. N., Ivison R. J., 2005, ApJ, 632, 736

Alexander D. M. et al., 2008, ApJ, 687, 835

Antonucci R., 1993, ARA&A, 31, 473

Antonucci R. R. J., Miller J. S., 1985, ApJ, 297, 621

Barger A. J. et al., 2003, AJ, 126, 632

Bassani L., Dadina M., Maiolino R., Salvati M., Risaliti G., della Ceca R., Matt G., Zamorani G., 1999, ApJS, 121, 473

Bauer F. E., Alexander D. M., Brandt W. N., Schneider D. P., Treister E., Hornschemeier A. E., Garmire G. P., 2004, AJ, 128, 2048

Benson A. J., Bower R. G., Frenk C. S., Lacey C. G., Baugh C. M., Cole S., 2003, ApJ, 599, 38

Booth C. M., Schaye J., 2009, MNRAS, 398, 53

Bower R. G., Benson A. J., Malbon R., Helly J. C., Frenk C. S., Baugh C. M., Cole S., Lacey C. G., 2006, MNRAS, 370, 645

Brandl B. R. et al., 2006, ApJ, 653, 1129

Brandt W. N., Hasinger G., 2005, ARA&A, 43, 827

Daddi E. et al., 2007, ApJ, 670, 173

Dole H. et al., 2006, A&A, 451, 417

Donley J. L., Rieke G. H., Pérez-González P. G., Rigby J. R., Alonso-Herrero A., 2007, ApJ, 660, 167

Downes A. J. B., Peacock J. A., Savage A., Carrie D. R., 1986, MNRAS, 218, 31

Dwelly T., Page M. J., 2006, MNRAS, 372, 1755

Elvis M. et al., 1994, ApJS, 95, 1

Fiore F. et al., 2008, ApJ, 672, 94

Frayer D. T. et al., 2006, ApJL, 647, L9

Gebhardt K. et al., 2000, ApJ, 539, L13

Genzel R. et al., 1998, ApJ, 498, 579

Georgantopoulos I., Georgakakis A., Rowan-Robinson M., Rovilos E., 2008, A&A, 484, 671

Giacconi R. et al., 2002, ApJS, 139, 369

Granato G. L., De Zotti G., Silva L., Bressan A., Danese L., 2004, ApJ, 600, 580

Guainazzi M., Matt G., Perola G. C., 2005, A&A, 444, 119

Hasinger G., 2008, A&A, 490, 905

Hopkins P. F., Hernquist L., Cox T. J., Di Matteo T., Robertson B., Springel V., 2006, ApJS, 163, 1

Horst H., Gandhi P., Smette A., Duschl W. J., 2008, A&A, 479, 389

Huynh M. T., Pope A., Frayer D. T., Scott D., 2007, ApJ, 659, 305

Kauffmann G., Haehnelt M., 2000, MNRAS, 311, 576

Kennicutt R. C. Jr., 1998, ARA&A, 36, 189

Krabbe A., Böker T., Maiolino R., 2001, ApJ, 557, 626

Krolik J. H., Begelman M. C., 1988, ApJ, 329, 702

La Franca F. et al., 2005, ApJ, 635, 864

Lehmer B. D. et al., 2005, ApJS, 161, 21

Luo B. et al., 2008, ApJS, 179, 19

Lutz D., Maiolino R., Spoon H. W. W., Moorwood A. F. M., 2004, A&A, 418, 465

Magnelli B., Elbaz D., Chary R. R., Dickinson M., Le Borgne D., Frayer D. T., Willmer C. N. A., 2009, A&A, 496, 57

Magorrian J. et al., 1998, AJ, 115, 2285

Mainieri V., Bergeron J., Hasinger G., Lehmann I., Rosati P., Schmidt M., Szokoly G., Della Ceca R., 2002, A&A, 393, 425

Mainieri V. et al., 2005, A&A, 437, 805

Maiolino R., Shemmer O., Imanishi M., Netzer H., Oliva E., Lutz D., Sturm E., 2007, A&A, 468, 979

Malizia A., Bassani L., Stephen J. B., Di Cocco G., Fiore F., Dean A. J., 2003, ApJ, 589, L17

Marconi A., Hunt L. K., 2003, ApJ, 589, L21

McLure R. J., Dunlop J. S., 2002, MNRAS, 331, 795

Menéndez-Delmestre K. et al., 2007, ApJ, 655, L65

Menéndez-Delmestre K., Blain A. W., Smail I., M.Alexander D., Chapman S. C., Armus L., Frayer D., Ivison R. J., Teplitz H., 2009, ApJ, 699, 667

Mushotzky R. F., Done C., Pounds K. A., 1993, ARA&A, 31, 717

Papovich C. et al., 2007, ApJ, 668, 45

Pope A. et al., 2006, MNRAS, 370, 1185

Pope A. et al., 2008, ApJ, 675, 1171

Richards G. T. et al., 2006, ApJS, 166, 470

Sanders D. B., Mirabel I. F., 1996, ARA&A, 34, 749

Silk J., Rees M. J., 1998, A&A, 331, L1

Springel V., Di Matteo T., Hernquist L., 2005, MNRAS, 361, 776

Stern D. et al., 2005, ApJ, 631, 163

Szokoly G. P. et al., 2004, ApJS, 155, 271

Tajer M. et al., 2007, A&A, 467, 73

Tozzi P. et al., 2006, A&A, 451, 457

Treister E., Krolik J. H., Dullemond C., 2008, ApJ, 679, 140

Tremaine S. et al., 2002, ApJ, 574, 740

Tueller J., Mushotzky R. F., Barthelmy S., Cannizzo J. K., Gehrels N., Markwardt C. B., Skinner G. K., Winter L. M., 2008, ApJ, 681, 113

Ueda Y., Akiyama M., Ohta K., Miyaji T., 2003, ApJ, 598, 886

Winter L. M., Mushotzky R. F., Reynolds C. S., Tueller J., 2009, ApJ, 690, 1322

## APPENDIX A: THE *SWIFT*-BAT COMPARISON SAMPLE

To aid in the interpretation of the *Spitzer* MIPS data used to characterize the CDF-S X-ray sample, we selected a local sample of AGNs from the *Swift*-BAT survey with *Spitzer*-IRS low-resolution spectroscopy (5.2–38 μm). The *Spitzer*-IRS data allows us to accurately distinguish between AGNs with AGN- and SB-dominated IR SEDs on the basis of the MIR spectral features in the *Swift*-BAT AGNs. The *Swift*-BAT survey provides the ideal local AGN comparison sample since the sensitivity of the BAT telescope to hard X-ray photons (14–195 keV) provides an almost absorption-independent selection of AGNs (to $N_H \approx 10^{24}$ cm$^{-2}$). Indeed, the range of X-ray luminosities and absorbing column densities of the *Swift*-BAT AGNs are comparable to those of the CDF-S AGNs (see Tueller et al. 2008; Winter et al. 2009); see Section 2.2.1.

36 of the 104 *Swift*-BAT AGNs with good-quality $L_{2-10\,keV}$ and $N_H$ constraints from Winter et al. (2009) or Bassani et al. (1999) have both Short–Low (SL; $3.6 \times 136.0$ arcsec$^2$; $R\sim 60$–127) and Long–Low (LL; $10.5 \times 360$ arcsec$^2$; $R \sim 57$–126) *Spitzer*-IRS spectroscopy, providing full coverage at 5.2–38 μm. All 36 BAT/IRS AGNs were observed in staring-mode with two nod positions, which are required for background subtraction. Basic calibrated data (BCD) images were combined and cleaned as described in Goulding & Alexander (2009). Differing nod positions were subtracted from each other to produce background subtracted images before extracting the spectra using SPICE.[11] The objects were sufficiently bright and the observations were sufficiently short that there was no significant effect from latent charge build-up on the detector. Long-slit orders were clipped using the wavelength trim ranges given in Table 5.1 of the *Spitzer*-IRS Observers Manual.[12] The continuum of each source in every order was fitted using a first or second-order polynomial. The spectra were then matched to give a single continuous spectrum for each source. Flux calibration was carried out using the latest available *Spitzer*-IRS calibration files (version 17.2) and is largely consistent with archival *IRAS* 25 μm

flux densities (to within a factor of 2.5 in ≈97 per cent of cases). The BAT/IRS AGNs have absorption corrected 2–10 keV luminosities spanning $4.3 \times 10^{41}$ to $1.9 \times 10^{44}$ erg s$^{-1}$ and absorbing column densities in the range $2.5 \times 10^{20}$ to $2.2 \times 10^{24}$ cm$^{-2}$ (i.e. roughly the same as those CDF-S X-ray AGN/SBs with $L_X$ and $N_H$ measurements published in Tozzi et al. 2006).

To determine whether the $S_{70}/S_{24}$ flux ratio can distinguish between SB- and AGN-dominated systems, we classified the BAT/IRS sample into those objects with (i) a prominent PAH feature at 6.2 μm, which we assume is a good indicator of a strong starburst component (SB-dominated; e.g. Genzel et al. 1998; 11 objects) and (ii) a power-law MIR to FIR continuum with no sign of any PAH feature at 6.2 μm, which we assume indicates an AGN-dominated object (25 objects). The 6.2 μm PAH feature is preferred over other lines as it lies in a region of the IR spectrum that is largely free of other strong spectral features, in particular the silicate absorption/emission band at 9.7 μm. We show the *Spitzer*-IRS spectra of the BAT/IRS sample in Fig. A1 (AGN-dominated systems) and Fig. A2 (SB-dominated systems).

To calculate the expected $S_{70}/S_{24}$ flux ratio tracks each of for the 36 BAT/IRS AGNs as a function of redshift, we shift each spectrum by a factor of $1 + z$ in wavelength (where $z$ is increased from 0.25 to 2.5 in steps of 0.025) and pass the resulting spectrum through the MIPS 24 and 70 μm filters. To determine the observed 70 μm fluxes at $z < 0.75$ requires knowledge of the IR SED beyond the wavelength coverage of the *Spitzer*-IRS spectra (i.e. >38 μm). To provide this longer wavelength coverage, we extrapolated the longest wavelength bin of the IRS spectra to the 60 and 100 μm flux densities from the *IRAS* Point Source and Faint Source Catalogues.[13] 32 of the 36 AGNs with IRS data have well constrained *IRAS* 60 and 100 μm fluxes. The remaining four (all classed as AGN dominated) have *IRAS* 60 or 100 μm flux densities that are flagged as upper limits in the *IRAS* catalogues. However, including these faint sources in our average AGN SED by assuming the upper limits as detections has no effect on any of our results. In Fig. A3, we show the $S_{70}/S_{24}$ flux ratios derived from the BAT/IRS sample as a function of redshift. There is a clear separation between AGN- and SB-dominated systems at $z \lesssim 1.5$, showing that the $S_{70}/S_{24}$ flux ratio can be used as an efficient method to determine whether AGN or star formation activity dominates the IR emission of X-ray detected AGNs.

Calculating $L_{IR}$ for high-redshift sources using the 24 μm flux density alone is susceptible to systematic errors caused by spectral features that are redshifted into this waveband at $z > 0.7$. We can use the BAT/IRS sample to establish the uncertainties in deriving $L_{IR}$ from either 70 or 24 μm data. In the lower panels of Fig. A3, we show the expected observed frame 70 and 24 μm fluxes for the BAT/IRS sample, if observed at $z = 0.25$–2.5 and normalized to $L_{IR} = 10^{12}$ L$_\odot$ (the normalization factor, $10^{12}$ L$_\odot/L_{IR}$, is derived by calculating $L_{IR}$ from the *IRAS* flux densities using the equations presented in table 1 of Sanders & Mirabel 1996). Depending on the shape of the IR SED, sources of the same $L_{IR}$ can differ in their observed 24 μm flux density by up to a factor of ≈12 at $z > 1$, compared to factor of only ≈3 at 70 μm. This range of 70 μm flux density is almost independent of redshift out to $z = 2.5$, indicating that $S_{70}$ is up four times more accurate for determining $L_{IR}$ when no information on the SED shape is available.
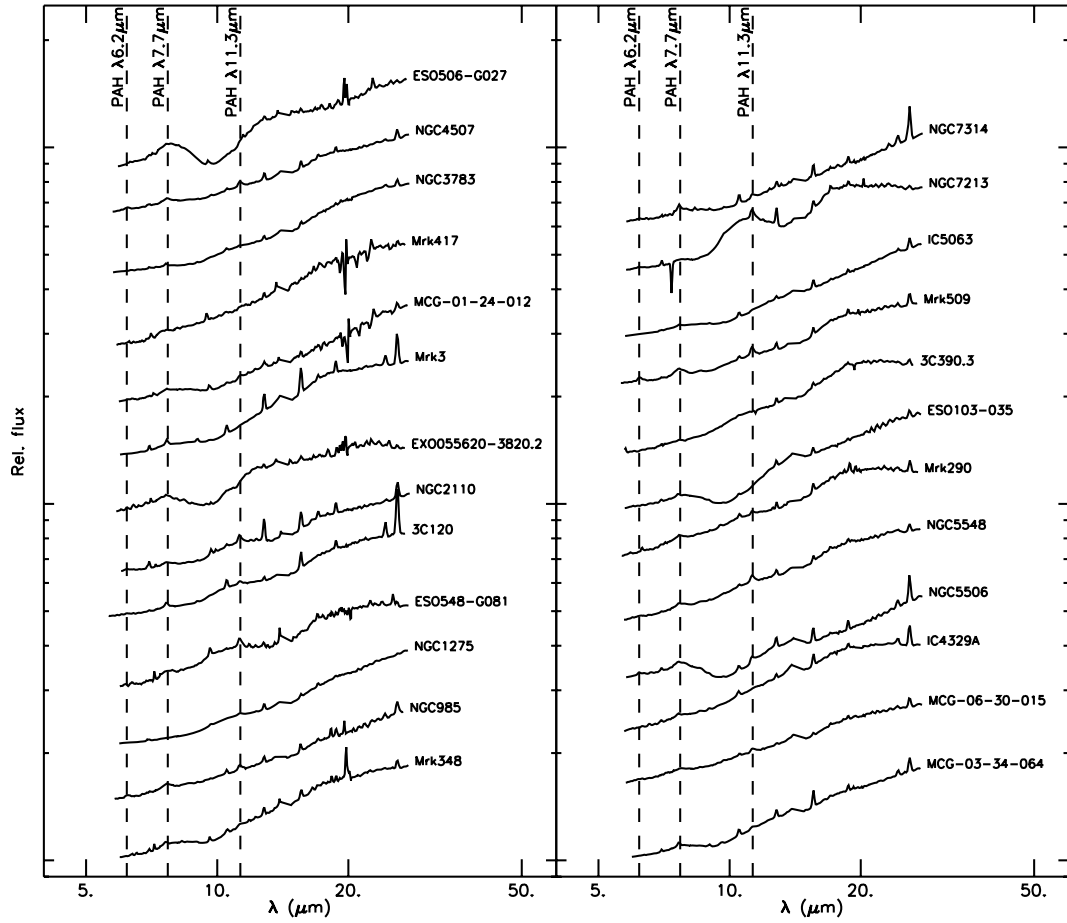
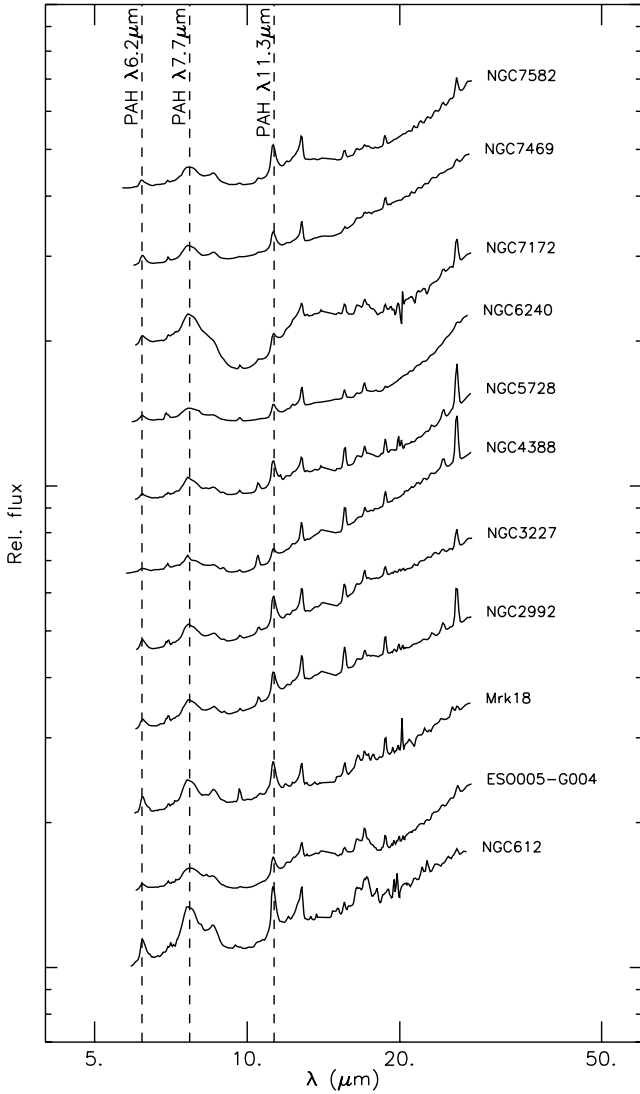**Figure A1.** IRS spectra of the 25 BAT/IRS AGNs that we classify as having AGN-dominated IR SEDs on the basis of the lack of a prominent PAH feature at 6.2 μm. Also indicated are the PAH features at 7.7 and 11.4 μm, although these were not used to distinguish between AGN- and SB-dominated systems.

**Figure A2.** IRS spectra of the 11 BAT/IRS AGNs that we classify as having SB-dominated IR SEDs on the basis of the presence of a prominent PAH feature at 6.2 μm. Also indicated are the PAH features at 7.7 and 11.4 μm, although these were not used to distinguish between AGN- and SB-dominated systems.
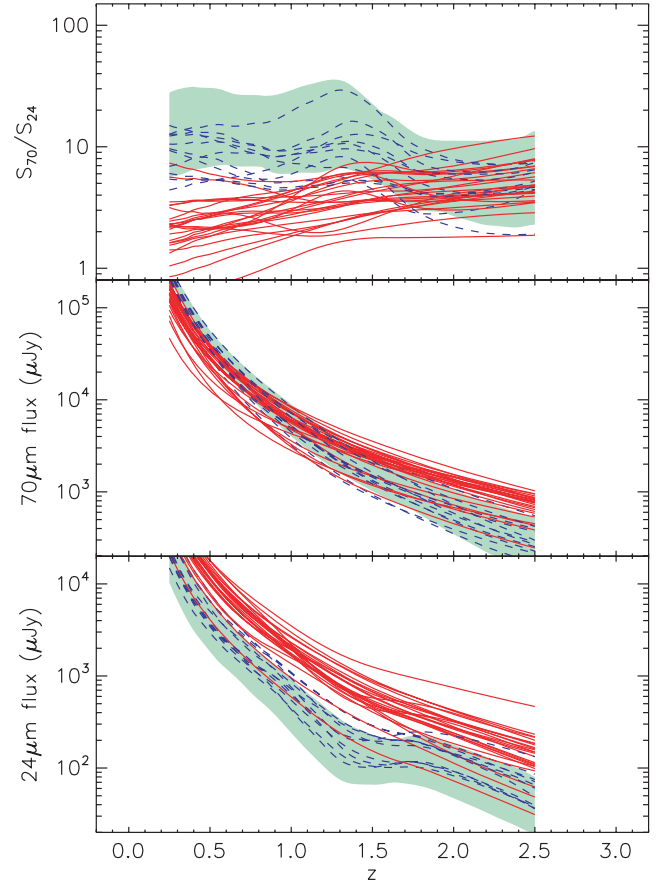


**Figure A3.** Top: the expected $S_{70}/S_{24}$ flux ratio of the AGNs in the BAT/IRS AGNs over the redshift range $z = 0.25$–2.5. Middle: the expected observed 70 μm flux densities of the BAT/IRS AGNs over the redshift range $z = 0.25$–2.5, each normalized to $L_{IR} = 10^{12}$ L$_{\odot}$. Bottom: the expected observed 24 μm flux densities of the BAT/IRS AGNs over the redshift range $z = 0.25$–2.5, again normalized to $L_{IR} = 10^{12}$ L$_{\odot}$. We show the ratios and flux densities as expected if the AGNs were to be observed at $z = 0.25$–2.5. Solid, red lines refer to AGN-dominated and dashed blue lines to SB-dominated AGNs. The green shaded areas indicate the spread of flux ratios and flux densities of the Brandl et al. (2006) starburst galaxies expected over the redshift range $z = 0.25$–2.5.

This paper has been typeset from a TeX/LaTeX file prepared by the author.